



1 A daily highest air temperature estimation method and  
2 spatial-temporal changes analysis of high temperature in  
3 China from 1979 to 2018

4 Ping Wang<sup>1,2\*</sup>, Kebiao Mao<sup>1,3\*</sup>, Fei Meng<sup>2</sup>, Zhihao Qin<sup>3</sup>, Shu Fang<sup>4</sup>, Sayed M. Bateni<sup>5</sup>,  
5 Mansour Almazroui<sup>6,7</sup>

6 <sup>1</sup> School of Physics and Electronic-Engineering, Ningxia University, Yinchuan 750021, China

7 <sup>2</sup> School of Surveying and Geo-Informatics, Shandong Jianzhu University, Jinan 250100, China

8 <sup>3</sup> Institute of agricultural resources and regional planning, Chinese Academy of Agricultural  
9 Sciences, Beijing 100081, China

10 <sup>4</sup> School of Earth Sciences and Resources, China University of Geosciences, Beijing 100083, China

11 <sup>5</sup> Department of Civil and Environmental Engineering and Water Resources Research Center,  
12 University of Hawaii at Manoa, Honolulu, HI 96822, USA

13 <sup>6</sup> Centre of Excellence for Climate Change Research/Department of Meteorology, King Abdulaziz  
14 University, Jeddah 21589, Saudi Arabia

15 <sup>7</sup> Climatic Research Unit, School of Environmental Sciences, University of East Anglia, Norwich,  
16 UK

17 Correspondence to: Kebiao Mao ([maokebiao@caas.cn](mailto:maokebiao@caas.cn))

18 ★ These authors contributed equally to this works.

19 **Abstract.** The daily highest air temperature ( $T_{max}$ ) is a key parameter for global and regional high  
20 temperature analysis, which is very difficult to be obtained in areas where there are no  
21 meteorological observation stations. This study proposes an estimation framework for obtaining  
22 high-precision  $T_{max}$ . Firstly, we build a near surface air temperature diurnal variation model to  
23 estimate  $T_{max}$  for China from 1979 to 2018 based on multi-source data. Then in order to further  
24 improve the estimation accuracy, we divided China into six regions according to climate conditions  
25 and topography, and established calibration models for different region. The analysis shows that the  
26 mean absolute error (MAE) of the dataset (<https://doi.org/10.5281/zenodo.5602897>) is about  
27 1.07 °C and RMSE is 1.52 °C, which improves the accuracy of the traditional method by nearly  
28 1 °C. The spatial-temporal variations analysis of  $T_{max}$  in China indicated that the annual and seasonal  
29 mean  $T_{max}$  in most areas of China showed an increasing trend. In summer and autumn, the  $T_{max}$  in



30 northeast China increased the fastest among the six regions, which were 0.4°C/10a and 0.39°C/10a,  
31 respectively. The number of summer days and warm days showed an increasing trend in all regions,  
32 while the number of icing days and cold days showed a decreasing trend. The abnormal temperature  
33 changes mainly occurred in El Niño years or La Niña years. We found that the influence of the  
34 Indian Ocean Basin Warming (IOBW) on air temperature in China were generally greater than those  
35 of the North Atlantic Oscillation and the NINO3.4 area sea surface temperature after making  
36 analysis of ocean climate modal indices with air temperature. In general, this  $T_{\max}$  dataset and  
37 analysis are of great significance to the study of climate change in China, especially for  
38 environmental protection.

39 **Keywords:** Near surface air temperature diurnal variation model; Daily highest air temperature; High temperature;  
40 Spatial-temporal analysis; Climate change

## 41 **1 Introduction**

42 In the context of global warming, the frequency of high temperature events is increasing, and high  
43 temperature tends to increase electricity demand and energy consumption (Zhang et al., 2021;  
44 Sathaye et al., 2013), adversely affecting human health, social economy and ecosystem (Sehra et al.,  
45 2020; Basu, 2009; Gasparrini and Armstrong, 2011). The daily highest air temperature ( $T_{\max}$ ) is the  
46 basic parameter for studying regional scale high-temperature events. It has a great influence on the  
47 ozone concentration (Abdullah et al., 2017; Kleinert et al., 2021) and the start time of the plant  
48 growth season (Yang et al., 2017).  $T_{\max}$  is not only an important factor for high temperature disaster  
49 risk assessment, but also a key input parameter for crop growth models and carbon emission model.  
50 Sustained and abnormally high  $T_{\max}$  will cause high temperature heat damage and adversely affect  
51 crop growth. Therefore, it is very important to accurately obtain the temporal and spatial distribution



52 of  $T_{\max}$  and study the characteristics of high temperature weather. Generally,  $T_{\max}$  is measured on a  
53 thermometer in a louvered box 1.5 meters above the ground in the field. Although the  $T_{\max}$  measured  
54 by this method has high accuracy but not spatial continuity. Therefore, some scholars spatialize the  
55 station based  $T_{\max}$  through methods such as Kriging interpolation and spline function interpolation.  
56 However, the number of meteorological stations is limited, and stations in remote areas and areas  
57 with complex terrain are even sparser, which makes the accuracy of  $T_{\max}$  obtained by interpolation  
58 difficult to meet the requirements of regional scale research in China.

59 In order to obtain information about the spatial distribution of the  $T_{\max}$ , many scholars began to  
60 use satellite remote sensing to solve this problem. There are three commonly remote sensing  
61 methods to estimate  $T_{\max}$ . The first method is regression analysis, which uses the correlation  
62 between land surface temperature (LST) and  $T_{\max}$  to establish a regression model to estimate  $T_{\max}$   
63 (Shen and Leptoukh, 2011; Evrendilek et al., 2012; Lin et al., 2012). The second method is machine  
64 learning, which can flexibly estimate  $T_{\max}$  in urban areas with complex features (Yoo et al., 2018).  
65 The third method is to use a diurnal temperature change model to extend the instantaneous air  
66 temperature ( $T_a$ ) to calculate  $T_{\max}$ , either by the Temperature-Vegetation Index (TVX) method  
67 (Wloczyk et al., 2011; Zhu et al., 2013), the energy balance method (Sun et al., 2005; Zhu et al.,  
68 2017), the atmospheric temperature profile extrapolation method (Fabiola and Mario, 2010), or  
69 other methods. The above methods of estimating  $T_{\max}$  with LST can better reflect the spatial  
70 distribution of  $T_{\max}$ , but regression analysis and machine learning require sufficient and  
71 representative samples, and the established model is not universal. TVX cannot estimate  $T_a$  at night  
72 and in sparse vegetation areas. Many parameters required by the energy balance method cannot  
73 usually be obtained by remote sensing technology. The estimation accuracy of atmospheric



74 temperature profile extrapolation method is greatly affected by the accuracy of the atmospheric  
75 temperature profile. Therefore, a new method for estimating  $T_{\max}$  needs to be proposed.

76 At present, most researches mainly use the extreme climate indices defined by the Expert Team  
77 on Climate Change Detection and Indices (ETCCDI) to analyze the temporal and spatial distribution  
78 characteristics of high temperature and its changing laws (Khan et al., 2018; Mcgree et al., 2019;  
79 Poudel et al., 2020; Ruml et al., 2017; Salman et al., 2017; Wang et al., 2019; Zhang et al., 2019).  
80 Zhou et al. (2016) analyzed the temperature indices changes in China from 1961 to 2010, and the  
81 results indicated that the warm extremes in China exhibited an increasing trend. In addition, the  
82 researchers analyzed the characteristics of high temperature changes in the Three River Headwaters,  
83 Yangtze River Basin, Loess Plateau, Inner Mongolia and Songhua River Basin (Ding et al., 2018;  
84 Guan et al., 2015; Sun et al., 2016; Tong et al., 2019; Zhong et al., 2017). In addition to analyzing  
85 the temporal and spatial changes of high temperature events, many scholars have also studied the  
86 influencing factors of high temperature events. Studies showed that extreme high temperature was  
87 related to abnormal atmospheric circulation disturbances (You et al., 2011; Zhong et al., 2017) and  
88 abnormal sea surface temperature (Li et al., 2019b; Wu et al., 2011). However, previous studies on  
89 the cause of high temperature events usually only analyzed the correlation between atmospheric  
90 circulation modes and the temperature indices along the time dimension, without considering the  
91 spatial characteristics of the correlation.

92 From the above analysis, most of the researches mainly use the meteorological observation  
93 temperature data interpolation to analyze local temperature changes, and almost no one constructs  
94 continuous high-temporal resolution  $T_{\max}$  for high temperature analysis in China. In order to better  
95 study regional high temperature events, this study proposes an estimation framework for obtaining





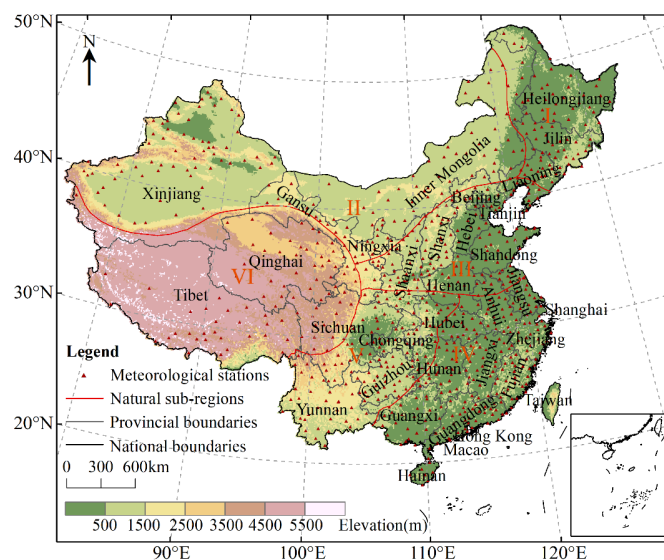
96 high-precision  $T_{\max}$ . Firstly, we used multi-source data and established near surface  $T_a$  diurnal  
97 variation model to build  $T_{\max}$  dataset in China from 1979 to 2018. To further improve the accuracy,  
98 we divided China into six regions according to climate conditions and topography, and established  
99 calibration models respectively. On this basis, we further analyzed the spatial-temporal variation  
100 characteristics of  $T_{\max}$  and corresponding influencing factors in China. This can provide evidence  
101 for mitigating global climate change and reducing regional carbon emissions for environmental  
102 protection.

## 103 **2 Study area**

104 In order to establish a more high-precision  $T_{\max}$  dataset to analyze the temporal and spatial  
105 characteristics of high-temperature in China, we divided the country into six regions based on  
106 topographic and climatic conditions, as shown in Fig.1. (I) The northeast region has a temperate  
107 monsoon climate. Affected by the monsoon,  $T_a$  is higher in winter in the southern part of the region,  
108 but it is the opposite in the northern part. The topography of this area is dominated by plains, hills,  
109 and mountains. Due to the influence of topography, the variability of  $T_a$  is large in local areas. (II)  
110 The northwestern region is dominated by a temperate continental climate (cold in winter and hot in  
111 summer) with a large annual and daily  $T_a$  range. The area is with little annual precipitation  
112 decreasing from east to west. The topography of this area is dominated by plateau basins and rivers  
113 are scarce. (III) North China is located in a semi-humid and humid zone in the warm temperate zone.  
114 Precipitation is mainly concentrated in summer. This area is dominated by plains and plateaus,  
115 bounded by Taihang Mountain, the Loess Plateau in the west, and the North China Plain in the east.  
116 (IV) The southeast region is dominated by mountains and hills, which belongs to the warm and  
117 humid subtropical oceanic monsoon climate zone, and the tropical monsoon climate zone. The



118 climate is mild, with an annual average  $T_a$  of 17-21°C and an average rainfall of 1400-2000mm. (V)  
119 The southwestern region has a subtropical monsoon climate, affected by the southeast monsoon and  
120 southwest monsoon. It is hot and rainy in summers, and the landforms in this area are dominated by  
121 plateaus and mountains. (VI) The Qinghai-Tibet Plateau is located in southwest China, with an  
122 average elevation of more than 4,000 meters. The towering terrain has a great impact on the climate  
123 in eastern and southwestern China. It has a plateau mountainous climate, with cold winters and  
124 warm summers, with aridity and little rain throughout the year.



125  
126

Figure 1. Overview of the study area.

### 127 3 Data

#### 128 3.1 China Meteorological Forcing Dataset (CMFD)

129 CMFD is developed by the Hydro-meteorological Research Group of the Institute of Tibetan Plateau  
130 Research, Chinese Academy of Sciences. The dataset can be obtained from the National Qinghai-  
131 Tibet Plateau Science Data Center (<https://data.tpsc.ac.cn/>). The near surface  $T_a$  data of CMFD has  
132 a time resolution of 3h and a spatial resolution of 0.1°, and its accuracy in China is better than Global



133 Land Data Assimilation System (GLDAS) data (He et al., 2020). The  $T_a$  data of CMFD have been  
134 widely used in climate simulation, hydrological simulation, vegetation greenness research, and  
135 cross-validation of new  $T_a$  datasets (Luan et al., 2020; Gu et al., 2020; Wang et al., 2020). Although  
136 this dataset has become one of the most widely used climate datasets in China, it does not provide  
137 the  $T_{max}$  value. In order to perform high temperature analysis, we need to construct a  $T_{max}$  dataset.

### 138 3.2 ERA5 data

139 ERA5 data is the fifth generation of global climate reanalysis data produced by the European Centre  
140 for Medium-range Weather Forecast (ECMWF) after ERA-Interim. The model version used by  
141 ERA5 is IFS Cycle 41r2, and its spatial-temporal resolution and number of vertical layers are much  
142 higher than the ERA-Interim data (Hoffmann et al., 2019; Urraca et al., 2018). ERA5 reanalysis  
143 data provide a variety of meteorological elements, including atmospheric parameters, land  
144 parameters, and ocean parameters, spanning a time range from 1950 to present. The data can be  
145 obtained from the ECMWF ERA5 data website (<https://cds.climate.copernicus.eu/>). The ERA5  
146 dataset also does not provide the  $T_{max}$ . This study used  $T_a$  data from 1979 to 2018 to help build a  
147  $T_{max}$  estimation model to generate  $T_{max}$  value.

### 148 3.3 Meteorological station data

149  $T_{max}$  data from the China Surface Climatic Data Daily Dataset (V3.0) from 1979 to 2018 were used  
150 to verify the accuracy of  $T_{max}$  estimations. The hourly  $T_a$  observation data from China  
151 meteorological stations were used to determine the occurrence times of  $T_{max}$  and daily lowest air  
152 temperature ( $T_{min}$ ). Both datasets are from CMA National Meteorological Information Center  
153 (<http://data.cma.cn/>). The data were subjected to preliminary quality control and evaluation by CMA,  
154 and all elements in the observational data are of high quality and completeness, with the validity



155 rate generally above 99%. These datasets have been widely used in Chinese climate research (Li et  
156 al., 2019a; Tong et al., 2019). To ensure the validity of the site data, manual checks were performed  
157 on all observed data, including extreme value tests and spatial-temporal consistency tests.

### 158 3.4 Ocean climate modal indices

159 The ocean occupies about 71% of the earth's surface area, which has a great impact on climate  
160 change. After considering the distribution characteristics of China's land and sea, we analyzed the  
161 effects of the following ocean climate modal indices on high temperature in China: Indian Ocean  
162 Basin warming (IOBW) index, North Atlantic Oscillation (NAO) index, and NINO3.4 area sea  
163 surface temperature (NINO3.4) index. Among them, the IOBW index comes from the National  
164 Climate Center of CMA (<http://cmdp.ncc-cma.net/cn/index.htm>), and the NAO index and NINO3.4  
165 index are from the National Oceanic and Atmospheric Administration of the United States  
166 (<https://psl.noaa.gov/data/climateindices/list/>). The time range of the three indices is 1979-2018, and  
167 the time scale is monthly.

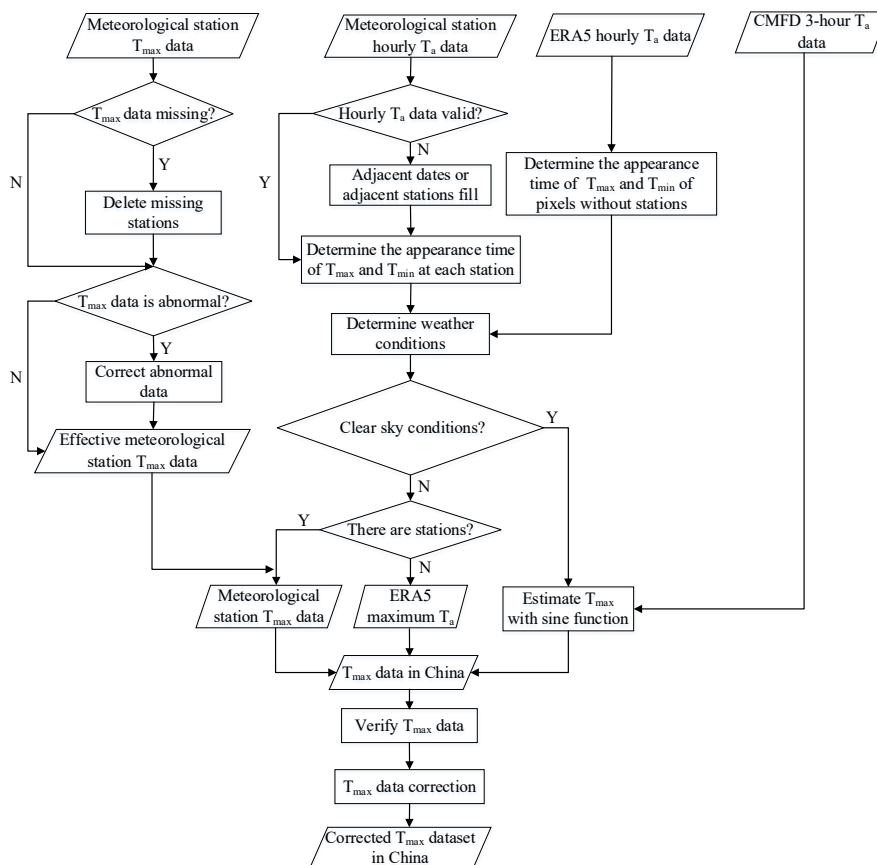
## 168 **4 Methodology**

### 169 4.1 $T_{\max}$ dataset construction

170 At present, the data used in the research on high temperature characteristics is mostly meteorological  
171 station data, or grid data obtained by interpolation of station data. A limited number of stations  
172 cannot represent the high temperature distribution at large scale. For regions where the stations are  
173 very sparse, grid data obtained by spatial interpolation can hardly meet the accuracy requirements  
174 of high temperature feature analysis. Although LST can be used to estimate  $T_{\max}$ , LST has degraded  
175 value in the presence of clouds or rainfall. Therefore, in order to obtain a  $T_{\max}$  dataset with high  
176 temporal and spatial resolution, we propose a  $T_{\max}$  construction model that combines meteorological



177 station data and reanalysis data, and considers the  $T_{\max}$  construction under clear sky and non-clear  
 178 sky conditions. The data processing process is shown in Fig. 2, and the data construction model is  
 179 divided into two steps:  $T_{\max}$  estimation and  $T_{\max}$  correction. First, the occurrence time of  $T_{\max}$  and  
 180  $T_{\min}$  was determined pixel by pixel. Then,  $T_{\max}$  was determined according to the weather state. (1)  
 181 In clear sky conditions, CMFD 3h near-surface  $T_a$  data was used to construct the  $T_a$  diurnal variation  
 182 model which in turn yielded  $T_{\max}$ . (2) In non-clear sky conditions, the site and reanalysis data were  
 183 used to fill pixels. Finally, the correction model was used to correct the poor quality pixels to  
 184 generate the final  $T_{\max}$  dataset in China.



185

186

Figure 2. Technical roadmap for  $T_{\max}$  estimation.

187 4.1.1  $T_{\max}$  estimation



188 The changes of  $T_a$  under different weather conditions are different. The changes of  $T_a$  under clear  
 189 sky conditions are relatively smooth and regular. Under non-clear sky conditions,  $T_a$  changes more  
 190 drastically. In order to improve the accuracy of  $T_{max}$  estimation, we determined the occurrence time  
 191 of  $T_{max}$  and  $T_{min}$  pixel by pixel. If there was a meteorological station at the pixel location, the analysis  
 192 could be divided into two situations. (1) If hourly  $T_a$  data was valid, it was directly used to determine  
 193 the occurrence time of  $T_{max}$  and  $T_{min}$ . (2) If there was a missing value in the hourly  $T_a$  data at a  
 194 certain time, then we used the valid data from adjacent stations at the same time or adjacent time at  
 195 the same stations to fill in the missing point. If there was no meteorological station at the pixel  
 196 location, we used ERA5 hourly  $T_a$  data to determine the occurrence time of  $T_{max}$  and  $T_{min}$ .

197 Studies have shown that the change of  $T_a$  under clear sky conditions follows a certain law: the  
 198 change curve of  $T_a$  during the day is close to a sine function (Ephrath et al., 1996; Johnson and  
 199 Fitzpatrick, 1977; Parton and Logan, 1981; Zhu et al., 2013), so we used it to simulate the change  
 200 of  $T_a$  during the day. The appearance time of  $T_{min}$  is  $t_{min}$ , and the appearance time of  $T_{max}$  is  $t_{max}$ .  
 201 According to the periodicity of the sine function, the model of the change of  $T_a$  during the day is  
 202 obtained like Eq. (1).

$$203 \quad T_a(t) = A \sin\left(\frac{\pi(t-t_{min})}{t_{max}-t_{min}} - \frac{\pi}{2}\right) + B \quad (1)$$

204 Use the least square method to solve the unknowns A and B:

$$205 \quad \begin{cases} \frac{\partial \delta}{\partial A} = \sum_{i=1}^n \left\{ 2 * \sin\left(\frac{\pi(t_i-t_{min})}{t_{max}-t_{min}} - \frac{\pi}{2}\right) * \left[ A * \sin\left(\frac{\pi(t_i-t_{min})}{t_{max}-t_{min}} - \frac{\pi}{2}\right) + B - T_{ai} \right] \right\} = 0 \\ \frac{\partial \delta}{\partial B} = \sum_{i=1}^n \left\{ 2 * \left[ A * \sin\left(\frac{\pi(t_i-t_{min})}{t_{max}-t_{min}} - \frac{\pi}{2}\right) + B - T_{ai} \right] \right\} = 0 \\ \delta = \sum_{i=1}^n \left[ A * \sin\left(\frac{\pi(t_i-t_{min})}{t_{max}-t_{min}} - \frac{\pi}{2}\right) + B - T_{ai} \right]^2 \end{cases} \quad (2)$$

206 Here  $n$  is the number of CMFD near surface  $T_a$  data used to construct the  $T_a$  change model in a  
 207 day. CMFD can obtain  $T_a$  data 8 times a day. This study uses four daytime  $T_a$  data to construct a  $T_a$   
 208 variation model, so  $n$  is 4.  $T_{ai}$  is the near surface  $T_a$  data at the  $i$ th time of CMFD, and  $\delta$  is the sum  
 209 of squares of the difference between the model estimated  $T_a$  and the near surface  $T_a$  of the CMFD.  
 210

211 Since the change of  $T_a$  under non-clear sky conditions does not conform to the sine curve change,  
 212 we divided the estimation of  $T_{max}$  under non-clear sky conditions into two situations. (1) If there  
 213 was a station at the location of the pixel, the measured  $T_{max}$  at the station was directly used as the



214  $T_{\max}$  of the pixel. (2) If there was no measured  $T_{\max}$  at the pixel location, the highest value of hourly  
215  $T_a$  of ERA5 in a day was taken as  $T_{\max}$ .

#### 216 4.1.2 $T_{\max}$ correction

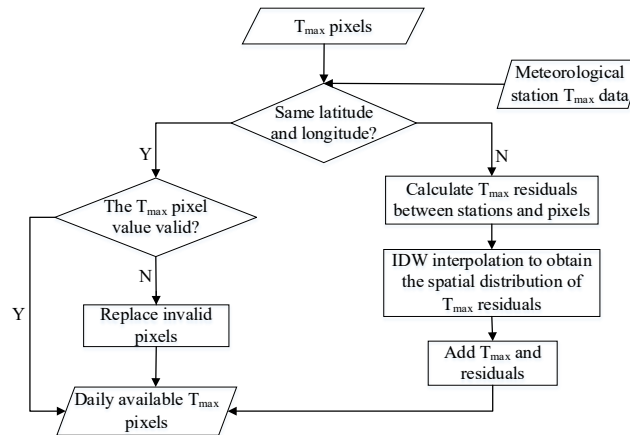
217 The validation of  $T_{\max}$  showed some differences between the estimated  $T_{\max}$  and the measured  $T_{\max}$ .  
218 In order to further improve the accuracy of  $T_{\max}$ , the measurements taken at weather stations should  
219 be used to correct the estimated  $T_{\max}$ , as shown in Fig. 3. For a pixel with poor quality, if there is  
220 station data at the location of the pixel, the low-quality pixel will be replaced with the measured  
221 data from the station. If there is no station data at the pixel location, the data is corrected by multiple  
222 linear regression method (Ninyerola et al., 2000; Zhao et al., 2020; Zheng et al., 2013). By  
223 establishing the regression relationship between station  $T_{\max}$  and estimated  $T_{\max}$ , the residuals were  
224 calculated according to the measured values and  $T_{\max}$  regression predicted values, and the spatial  
225 distribution of the residuals was obtained by the inverse distance weight (IDW) interpolation method.  
226 Finally, the estimated  $T_{\max}$  and the residual were added to obtain the corrected  $T_{\max}$ . The calibration  
227 model is like Eq. (3) and Eq. (4).

$$228 \quad T_{after}(i, j) = T_{before}(i, j) + \hat{\epsilon}(i, j) \quad (3)$$

$$229 \quad \hat{\epsilon}(i, j) = T_{true}(i, j) - T_{forecast}(i, j) \quad (4)$$

230 Here  $i$  and  $j$  are the row and column numbers of the image,  $T_{after}(i, j)$  is  $T_{\max}$  after correction,  
231  $T_{before}(i, j)$  is  $T_{\max}$  before correction,  $\hat{\epsilon}(i, j)$  is the residual,  $T_{true}(i, j)$  is the measured  $T_{\max}$ , and  
232  $T_{forecast}(i, j)$  is  $T_{\max}$  predicted by the regression model.

233 We used the jackknife method to randomly divide the station data into calibration and  
234 verification data (Benali et al., 2012; Zhao et al., 2020). We selected 80% of the meteorological  
235 stations to establish the regression relationship between the measured and estimated  $T_{\max}$  values.  
236 The other 20% of the meteorological stations were used to verify the accuracy of the corrected data.  
237 In order to improve data accuracy, the dataset used in the subsequent analysis of spatial-temporal  
238 variation of high temperature was the data corrected by all stations. Due to the different topographic  
239 and climatic characteristics of the six natural regions, the linear models of estimated  $T_{\max}$  and  
240 measured  $T_{\max}$  in each region were different. In order to obtain a higher-precision correction, the six  
241 regions were corrected separately.



242  
 243

Figure 3. Flow chart of  $T_{\max}$  correction.

244 4.2 Trend analysis

245 4.2.1 Sen's slope estimation

246 In this study, the trends of  $T_{\max}$  and extreme temperature indices were calculated using Sen's slope  
 247 estimation. Sen's slope estimation is a nonparametric estimation method. Even if there are some  
 248 outliers in the sample, it can reliably estimate the change trend of the time series, so it is widely used  
 249 in trend analysis (Sen, 1968; Zhang et al., 2017). The Eq. (5) is used to calculate the slope of each  
 250 pair of data.

251 
$$K_i = \frac{x_k - x_j}{k - j} \quad (i = 1, 2, \dots, N) \quad (5)$$

252 Where  $N = \frac{n(n-1)}{2}$ ,  $x_k$  and  $x_j$  are the time series values of the  $k$ th and  $j$ th samples respectively  
 253 ( $1 \leq j < k \leq n$ ). Arranging the  $N$ ,  $K_i$  values in ascending order, the median Sen's slope is  
 254 estimated as Eq. (6).

255 
$$\text{Slope} = \begin{cases} K_{[(N+1)/2]} & , N \text{ is odd} \\ \frac{K_{[N/2]} + K_{[(N+2)/2]}}{2} & , N \text{ is even} \end{cases} \quad (6)$$

256 4.2.2 Mann-Kendall trend test

257 Mann-Kendall trend test is used to test the trends of  $T_{\max}$  and extreme temperature indices. Mann-  
 258 Kendall method does not require samples to follow a certain distribution and is not disturbed by a  
 259 few outliers, and it can test the change trend of time series (Seenu and Jayakumar, 2021; Tan et al.,  
 260 2019). Eq. (7) is used to calculate the statistic of the Mann-Kendall trend test.





261 
$$S = \sum_{i=1}^{n-1} \sum_{j=i+1}^n \text{sgn}(x_j - x_i) \quad (7)$$

262 
$$\text{sgn}(x_j - x_i) = \begin{cases} 1, & x_j - x_i > 0 \\ 0, & x_j - x_i = 0 \\ -1, & x_j - x_i < 0 \end{cases} \quad (8)$$

263 
$$\text{Var}(S) = \frac{n(n-1)(2n+5)}{18} \quad (9)$$

264 Here  $x_i$  and  $x_j$  are the  $i$ th and  $j$ th data values of the time series, and  $n$  is the length of the time  
 265 series, where  $n$  is 40.  $\text{Var}(S)$  is the variance of  $S$ . The standardized statistic  $Z_c$  is computed by using  
 266 Eq. (10).

267 
$$Z_c = \begin{cases} \frac{S-1}{\sqrt{\text{Var}(S)}}, & S > 0 \\ 0, & S = 0 \\ \frac{S+1}{\sqrt{\text{Var}(S)}}, & S < 0 \end{cases} \quad (10)$$

268 When  $|Z_c| > Z_{1-\alpha/2}$ , the change trend is considered to be significant. Here,  $Z_{1-\alpha/2}$  is the  
 269 standard normal variance,  $\alpha$  is the significance test level, when  $\alpha = 0.05$ ,  $Z_{1-\alpha/2} = 1.96$ , and  
 270 when  $\alpha = 0.01$ ,  $Z_{1-\alpha/2} = 2.58$ .

271 **4.3 Mann-Kendall test for abrupt change analysis**

272 Climate system change is an unstable and discontinuous change process, and one of the commonly  
 273 used methods to test its change is the Mann-Kendall mutation test, which is very effective in testing  
 274 the change of elements from a relatively stable state to another state (Ruml et al., 2017). For a time  
 275 series  $x$  with  $n$  samples, Eq. (11) is used to construct an ordered sequence.

276 
$$s_k = \sum_{i=1}^k r_i \quad (k = 2, 3, \dots, n) \quad (11)$$

277 
$$r_i = \begin{cases} +1, & x_i > x_j \\ 0, & x_i \leq x_j \end{cases} \quad (j = 1, 2, \dots, i) \quad (12)$$

278 
$$UF_k = \frac{s_k - E(s_k)}{\sqrt{\text{Var}(s_k)}} \quad (k = 1, 2, \dots, n) \quad (13)$$

279 
$$E(s_k) = \frac{k(k-1)}{4} \quad (14)$$

280 
$$\text{Var}(s_k) = \frac{k(k-1)(2k+5)}{72} \quad (15)$$

281 Where  $s_k$  is the cumulative count of the number of values at time  $i$  greater than that at time  $j$ .  
 282  $E(s_k)$  and  $\text{Var}(s_k)$  are the mean and variance of the cumulative number  $s_k$  respectively.  $UF_k$  is a



283 standard normal distribution, given the significance level  $\alpha$ , and may be obtained from the normal  
 284 distribution table. If  $|UF_k| > U_\alpha$ , which indicates that there is an obvious trend change in the  
 285 sequence. Reverse the time series  $x$  to  $x_n, x_{n-1}, \dots, x_1$ , and repeat the above process with  $UB_k =$   
 286  $-UF_k(k = n, n - 1, \dots, 1)$ .

#### 287 4.4 Extreme temperature indices

288 ETCCDI proposed a set of extreme climate indices in the Climate Change Monitoring conference,  
 289 which became the unified standard for climate change research (Hong and Ying, 2018; Mcgree et  
 290 al., 2019; Poudel et al., 2020; Zhang et al., 2019; Zhou et al., 2016). Among them, 27 indices are  
 291 considered as core indices, which are calculated from daily  $T_a$  and precipitation data and have the  
 292 characteristics of weak extremeness, low noise, and strong significance. These indices  
 293 comprehensively capture the frequency, intensity and duration of extreme climate events, and are  
 294 recommended as the core indicators for extreme climate event analysis by the STARDEX program  
 295 of the European Union (Guan et al., 2015; Ruml et al., 2017). In this study, six temperature indices  
 296 related to  $T_{\max}$  were used to analyze high temperature characteristics, and their definitions are shown  
 297 in Table 1.

298 **Table 1.** Definition of extreme temperature indices.

| Index | Name               | Definition  | Category  | Unit             |
|-------|--------------------|---|-----------|------------------|
| SU    | Summer days        | Annual count of days when $T_{\max} > 25^\circ\text{C}$ | Frequency | d                |
| TX90p | Warm days          | Annual count of days when $T_{\max} > 90$ th percentile | Frequency | d                |
| TXn   | Minimum $T_{\max}$ | Annual minimum value of $T_{\max}$                      | Intensity | $^\circ\text{C}$ |
| TXx   | Maximum $T_{\max}$ | Annual maximum value of $T_{\max}$                      | Intensity | $^\circ\text{C}$ |
| ID    | Icing days         | Annual count of days when $T_{\max} < 0^\circ\text{C}$  | Frequency | d                |
| TX10p | Cold days          | Annual count of days when $T_{\max} < 10$ th percentile | Frequency | d                |

#### 299 4.5 Correlation analysis

300 Pearson correlation coefficient is often used to accurately measure the degree of correlation between  
 301 two variables, and its size can reflect the strength of the correlation of the variables (Cao et al., 2020;  
 302 Yan et al., 2021). For variables  $x_1, x_2, \dots, x_n$  and variables  $y_1, y_2, \dots, y_n$ , the correlation coefficient  
 303 between them is calculated as Eq. (16).



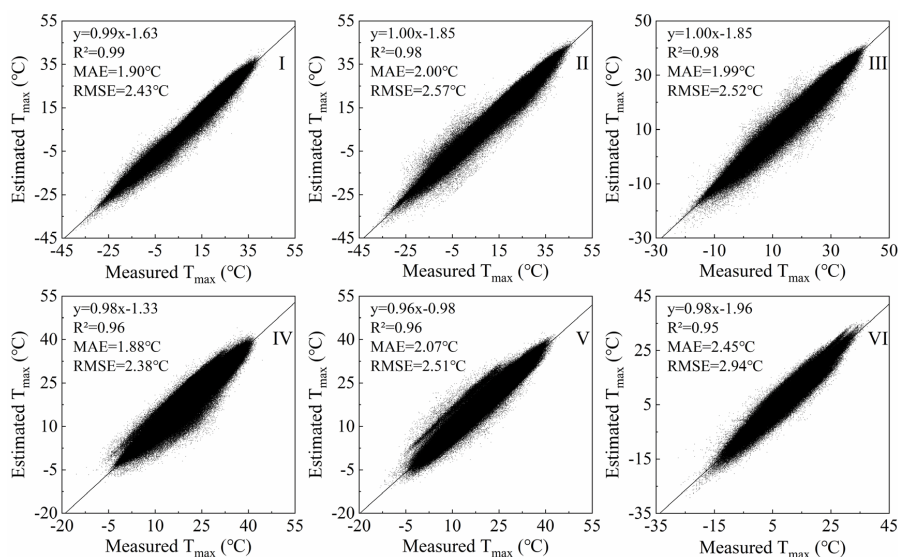
304 
$$R = \frac{n \sum_{i=1}^n (x_i \times y_i) - \sum_{i=1}^n x_i \sum_{i=1}^n y_i}{\sqrt{n \sum_{i=1}^n x_i^2 - (\sum_{i=1}^n x_i)^2} \sqrt{n \sum_{i=1}^n y_i^2 - (\sum_{i=1}^n y_i)^2}} \quad (16)$$

305 Here  $n$  is the total length of the time series. The value of the correlation coefficient  $R$  is between  
306  $-1$  and  $1$ .  $R < 0$  indicates a negative correlation.  $R > 0$  indicates a positive correlation. The closer the  
307 absolute value of  $R$  is to  $1$ , the closer the relationship between the two elements is.

## 308 5 Results

### 309 5.1 Validation

310 In order to verify the feasibility of  $T_{\max}$  estimation using the  $T_a$  diurnal variation model and to  
311 analyze the accuracy of  $T_{\max}$  estimation in different regions, scatter plots of estimated  $T_{\max}$  and  
312 measured  $T_{\max}$  in six natural regions (I, II, III, IV, V and VI) were drawn according to the regional  
313 division in Fig. 1. The results are shown in Fig. 4, and the validation in each region shows that the  
314 root mean square errors (RMSE) is between  $2.38$ - $2.94^\circ\text{C}$ , and the mean absolute error (MAE) is  
315 between  $1.88$ - $2.45^\circ\text{C}$ , and the coefficient of determination ( $R^2$ ) is between  $0.95$ - $0.99$ . Among them,  
316 the accuracy in region IV is the highest, while the accuracy is the lowest in region VI. As can be  
317 seen from Fig. 4, although most of the data is very accurate, some have some room for improvement.  
318 Therefore, further correction is needed to improve the accuracy of the  $T_{\max}$  dataset.



319

320

**Figure 4.** Validation of  $T_{\max}$  estimation results in each region.

321

322

323

324

325

326

327

328

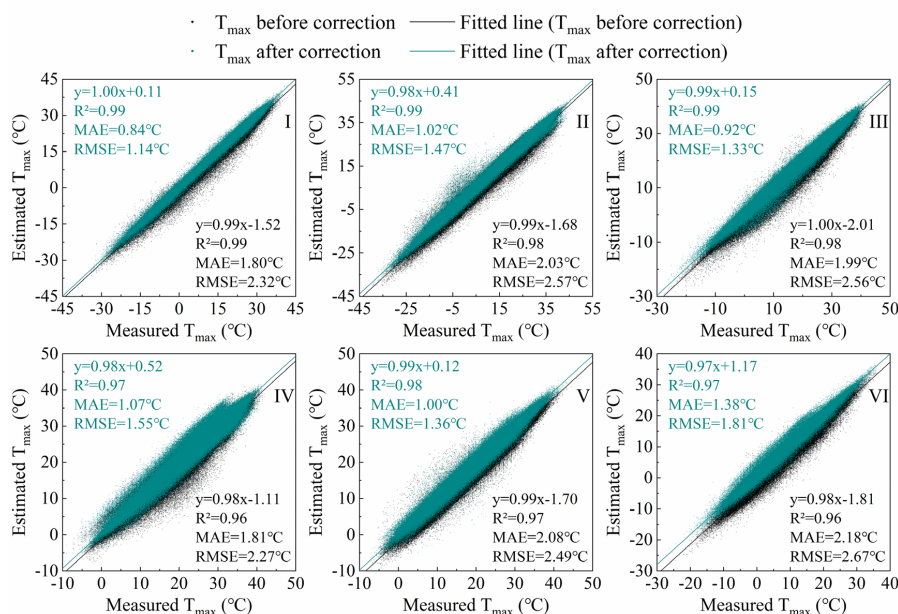
329

330

331

332

The correction method in Sect. 4.1.2 was used to correct the  $T_{\max}$  estimation results of six regions separately. The comparison between  $T_{\max}$  before and after correction with the measured  $T_{\max}$  is shown in Fig. 5. It can be seen that  $T_{\max}$  corrected by the regression model is more consistent with the measured  $T_{\max}$ . The RMSE decreases from 2.38-2.94°C to 1.14-1.81°C, and the MAE decreases from 1.88-2.45°C to 0.84-1.38°C, and the  $R^2$  increases from 0.96-0.99 to 0.97-0.99. The accuracy of  $T_{\max}$  is improved in each region after correction. The number of meteorological stations in region I is denser, and the accuracy of  $T_{\max}$  after calibration is significantly improved. The RMSE reduced from 2.32°C to 1.14°C, and the error is reduced by 51%. The number of meteorological stations in region VI is small, and the topography is undulating and the spatial heterogeneity is large. Therefore, the accuracy in this region is still the lowest among the six natural areas after correction. In general, the corrected  $T_{\max}$  dataset has higher consistency with the measured data, and which can be applied to research related to regional scale  $T_{\max}$ .



333

334

Figure 5. Validation of  $T_{\max}$  after correction.

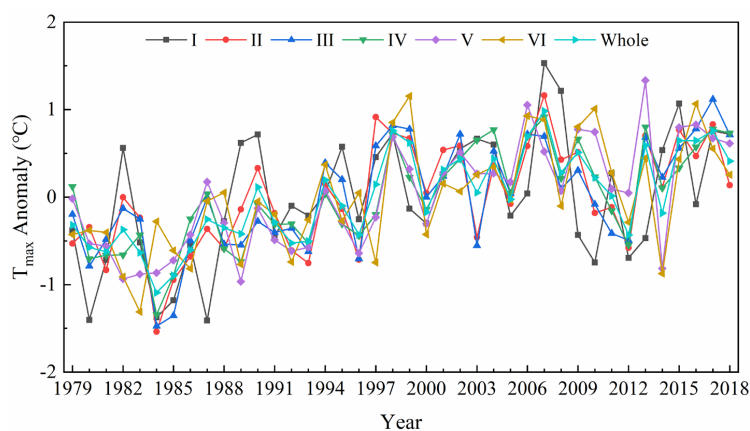
335 5.2 Temporal and spatial changes of  $T_{\max}$

336 5.2.1 Inter-annual variability

337 Fig. 6 shows the annual average change of  $T_{\max}$  in each region of China during 1979-2018. The  $T_{\max}$   
 338 in each region exhibited an upward trend. However, due to the different geographical locations and  
 339 the influence of atmospheric circulation in various regions, the change of  $T_{\max}$  was also different.  
 340 The order of the  $T_{\max}$  increase in each region was: V>IV>III>Whole>VI>II>I. The  $T_{\max}$  anomaly  
 341 ranges of region I-VI and the whole China region were -1.41-1.53, -1.54-1.16, -1.47-1.12, -1.34-  
 342 0.92, -0.97-1.33, -1.31-1.15, and -1.09-0.98°C, respectively. The  $T_{\max}$  variation coefficients were  
 343 0.082, 0.045, 0.036, 0.024, 0.03, 0.088 and 0.038, respectively. It can be seen that  $T_{\max}$  fluctuated  
 344 the most in region VI and the least in region IV. The minimum values of region I-VI and China  
 345 region appeared in 1987, 1984, 1984, 1984, 1989, 1983, and 1984, respectively which were  
 346 distributed in the 1980s. The highest values of  $T_{\max}$  appeared in 2007, 2007, 2017, 2007, 2013, 1999,



347 and 2007 respectively. Zhai et al. (2016) found that 1999, 2007, and 2013 were among the 10 years  
348 with the highest average  $T_a$  in China from 1900 to 2015. From 1998 to 2012, global surface  
349 temperature experienced a warming hiatus (Du et al., 2019; Li et al., 2015), and  $T_{max}$  in all regions  
350 of China showed a downward trend during this period.



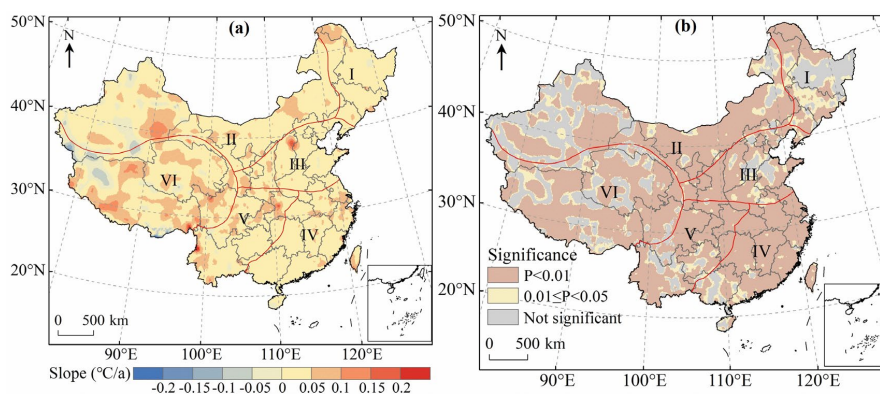
351

352 **Figure 6.** Inter-annual changes of  $T_{max}$  anomalies in six regions of China during 1979-2018.

353 In order to understand the spatial pattern and regional differences of  $T_{max}$  changes with more  
354 detail in China, Sen's slope estimation was used to calculate the annual average  $T_{max}$  change rate  
355 from 1979 to 2018 at the pixel scale (Fig. 7a). The significance test of the  $T_{max}$  change trend was  
356 conducted by the Mann-Kendall trend test (Fig. 7b). At the same time, the average change rate of  
357  $T_{max}$  in each region and the area percentage of significant increase and decrease of  $T_{max}$  were  
358 calculated (Table 2). The results indicated that the annual average  $T_{max}$  change rate in most regions  
359 of China (78.24% of the study area) passed the significance test with a confidence of 0.05, and 65.84%  
360 of the pixels showed very significant changes in  $T_{max}$  ( $P < 0.01$ ). Fig. 7a showed that the annual  
361 average  $T_{max}$  in most regions of China was on the rise, and the fastest rising rate of  $T_{max}$  was in  
362 western Yunnan. Only 8.13% of the regions in China showed a downward trend in  $T_{max}$ . These were  
363 concentrated mainly in the north and south of Xinjiang, and the northwest and south of Tibet.



364 Among the six regions, the average  $T_{\max}$  change rate of region V was the largest ( $0.38^{\circ}\text{C}/10\text{a}$ ), and  
 365 the average  $T_{\max}$  change rate of region I and region II was the lowest ( $0.31^{\circ}\text{C}/10\text{a}$ ) (Table 2).



366  
 367 **Figure 7.** Inter-annual change rate of  $T_{\max}$  (a) and results of Mann-Kendall trend test (b).

368 **Table 2.** Statistics of  $T_{\max}$  change trends in various regions of China from 1979 to 2018.

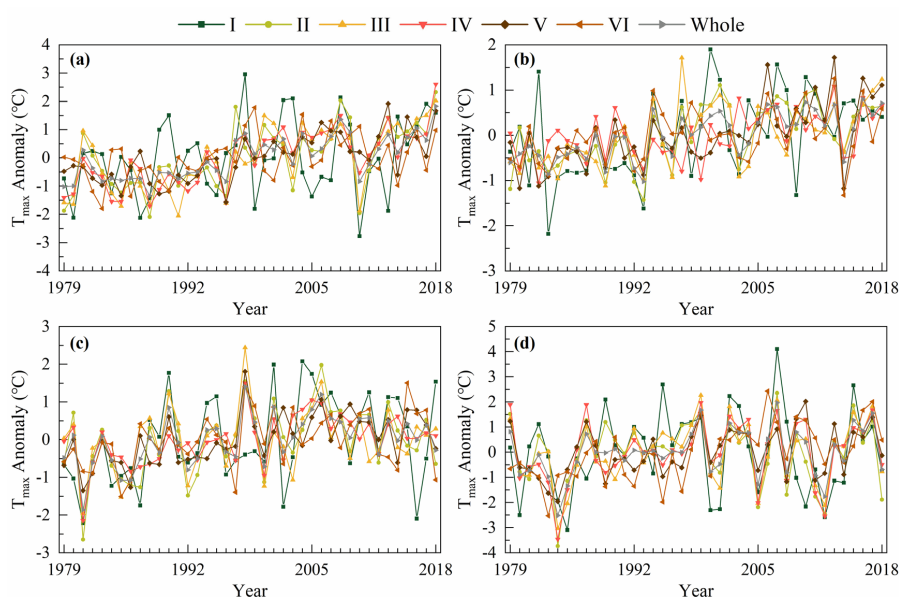
| Region                                 | I     | II    | III   | IV    | V     | VI    | Whole |
|--|-------|-------|-------|-------|-------|-------|-------|
| Mean ( $^{\circ}\text{C}/10\text{a}$ ) | 0.31  | 0.31  | 0.33  | 0.35  | 0.38  | 0.33  | 0.33  |
| Significant upward (%)                 | 65.21 | 69.45 | 87.03 | 92.29 | 87.00 | 67.93 | 75.13 |
| Significant downward (%)               | 0.09  | 3.14  | 0     | 0.32  | 0.75  | 7.92  | 3.11  |

369 5.2.2 Seasonal changes

370 On the basis of the annual analysis, we also analyzed the seasonal changes. The seasons are divided  
 371 according to the months (spring from March to May, summer from June to August, autumn from  
 372 September to November, and winter from December to February). We plotted the seasonal variation  
 373 curve of  $T_{\max}$  in China from 1979 to 2018 (Fig. 8), and some information on the trend of  $T_{\max}$   
 374 changes is shown in Table 3. The results indicated that  $T_{\max}$  in each region fluctuated the most in  
 375 winter and the least in summer. The highest  $T_{\max}$  in each region in spring, summer, autumn and  
 376 winter mostly occurred in 2018, 2013, 1998 and 2007, while the minimum  $T_{\max}$  in each region in  
 377 spring, summer, autumn and winter mostly occurred in 1988, 1993, 1981 and 1984. In 2013,  $T_{\max}$



378 of region IV-VI in summer reached the highest since 1979, mainly due to the influence of the  
379 southwest monsoon, East Asian summer monsoon and other factors. Under the influence of El Niño,  
380  $T_{\max}$  in winter in region I, II and the whole study area was the highest in 2007. Under the influence  
381 of La Niña, the minimum  $T_{\max}$  in spring and winter in most areas of China appeared in 1988 and  
382 1984, respectively. In the same season, the variation trend of  $T_{\max}$  in each region was significantly  
383 different, and some even had opposing trends. However, influenced by La Niña and the Eurasian  
384 atmospheric circulation,  $T_{\max}$  in winter in each region showed a consistent decreasing trend from  
385 2007 to 2008. As can be seen from Table 3, the regions with the fastest  $T_{\max}$  rise in spring, summer,  
386 autumn and winter are III, I, I and VI respectively, and the regions with the lowest  $T_{\max}$  change rate  
387 are VI, VI, III and II respectively. We found that  $T_{\max}$  in winter of region II exhibited a very slight  
388 downward trend, but the sliding average of the 3-year and 5-year unit exhibited a weak upward trend.



389  
390 **Figure 8.** Changes of  $T_{\max}$  anomalies in various regions of China in spring (a), summer (b), autumn (c), winter (d)  
391 during 1979-2018.

392 **Table 3.** Seasonal variation trend of  $T_{\max}$  in various regions of China from 1979 to 2018.

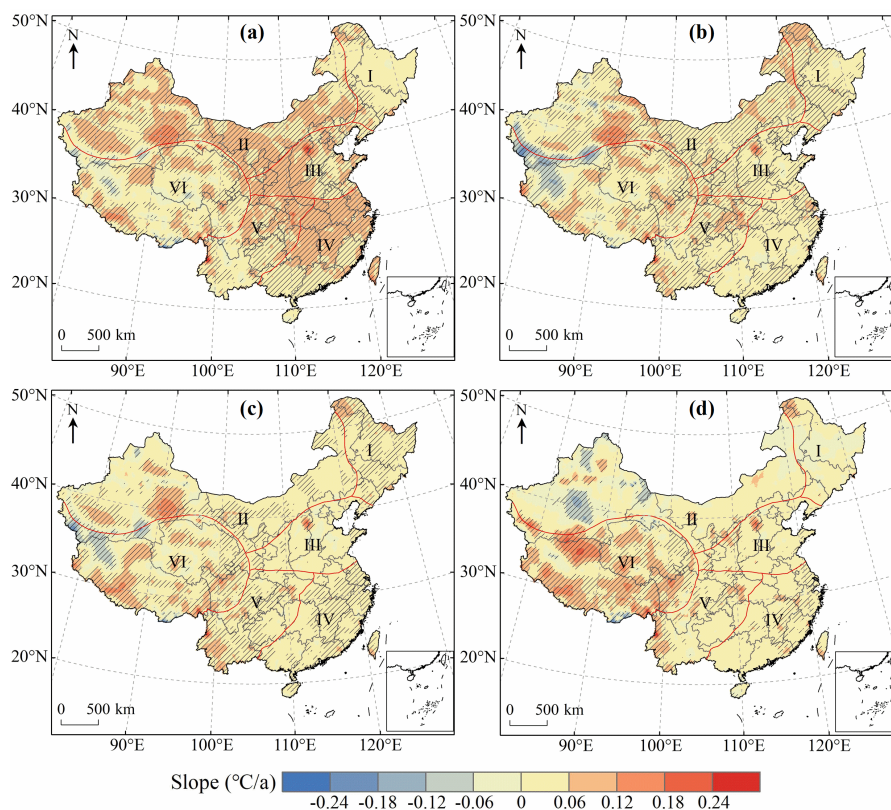




|        | I       | II      | III     | IV      | V       | VI      | Whole   |
|--------|---------|---------|---------|---------|---------|---------|---------|
| Spring | 0.035   | 0.063** | 0.072** | 0.063** | 0.051** | 0.026*  | 0.048** |
| Summer | 0.040** | 0.035** | 0.033** | 0.022** | 0.039** | 0.020*  | 0.031** |
| Autumn | 0.039*  | 0.024   | 0.014   | 0.025** | 0.035** | 0.025*  | 0.023** |
| Winter | 0.009   | -0.002  | 0.027   | 0.037   | 0.034*  | 0.058** | 0.027   |

393 (\*, \*\* represent the trends are significant at the level of  $p=0.05$ ,  $p=0.01$ , respectively.)

394 In order to display the seasonal variation characteristics of  $T_{\max}$  in China more intuitively, we  
395 drew the spatial distribution of the trend of  $T_{\max}$  and conducted a significance test (Fig. 9).  
396 Meanwhile, we counted the percentage of significant increase and decrease of  $T_{\max}$  in each region  
397 (Table 4). The results indicated that the areas with increasing  $T_{\max}$  were more than those with  
398 decreasing  $T_{\max}$  in all seasons. From 1979 to 2018, the increasing trend of  $T_{\max}$  was most significant  
399 in spring, which accounted for 92.73% of the total study area, followed by autumn and summer,  
400 while  $T_{\max}$  increased the least in winter. Specifically,  $T_{\max}$  increased significantly in most parts of  
401 China in spring, and the region where  $T_{\max}$  decreased significantly were mainly concentrated in the  
402 region VI (Fig. 9a). In summer,  $T_{\max}$  in most part of China showed a significant increasing trend,  
403 but  $T_{\max}$  in southern Xinjiang and northwestern Tibet exhibited a decreasing trend (Fig. 9b).  
404 Compared with spring and summer, the area with a significant increasing trend of  $T_{\max}$  in autumn  
405 was smaller, and the regions with a significant decreasing trend of  $T_{\max}$  were mainly distributed in  
406 Xinjiang and Tibet (Fig. 9c). 79.02% of the regions experienced an increase in  $T_{\max}$  in winter, which  
407 was significantly lower than in other seasons. A significant increasing trend of  $T_{\max}$  was observed  
408 in the east of region IV, the southwest of regions V and VI, while the areas where  $T_{\max}$  decreased  
409 significantly were mainly observed in Xinjiang (Fig. 9d). We also observed no significant decrease  
410 in  $T_{\max}$  in regions I and III in spring, I in summer, I and IV in autumn, and III in winter (Table 4).  
411 Further statistics showed that  $T_{\max}$  of the whole region III showed an upward trend in spring.



412

413

**Figure 9.** Spatial distribution of the change trend of  $T_{\max}$  in spring (a), summer (b), autumn (c), winter (d) over

414

China during 1979-2018. The shaded areas indicate trends that are statistically significant at the 0.05 level.

415

**Table 4.** Change trend statistics of  $T_{\max}$  in different seasons over China from 1979 to 2018.

|       | Significant upward (%) |        |        |        | Significant downward (%) |        |        |        |
|-------|------------------------|--------|--------|--------|--------------------------|--------|--------|--------|
|       | Spring                 | Summer | Autumn | Winter | Spring                   | Summer | Autumn | Winter |
| I     | 35.12                  | 74.75  | 65.75  | 6.89   | 0                        | 0      | 0      | 0.10   |
| II    | 81.56                  | 73.47  | 36.07  | 8.10   | 1.01                     | 7.04   | 3.15   | 10.87  |
| III   | 97.71                  | 69.05  | 14.67  | 15.99  | 0                        | 0.38   | 0.06   | 0      |
| IV    | 96.20                  | 46.80  | 57.26  | 29.47  | 0.35                     | 0.68   | 0      | 0.44   |
| V     | 76.48                  | 75.11  | 58.56  | 31.62  | 1.24                     | 1.53   | 0.06   | 0.12   |
| VI    | 50.20                  | 55.11  | 49.54  | 68.58  | 7.00                     | 14.17  | 10.34  | 2.28   |
| Whole | 71.46                  | 65.39  | 45.86  | 29.40  | 2.29                     | 6.04   | 3.61   | 4.01   |

416

### 5.3 Temporal and spatial changes of extreme temperature indices

417

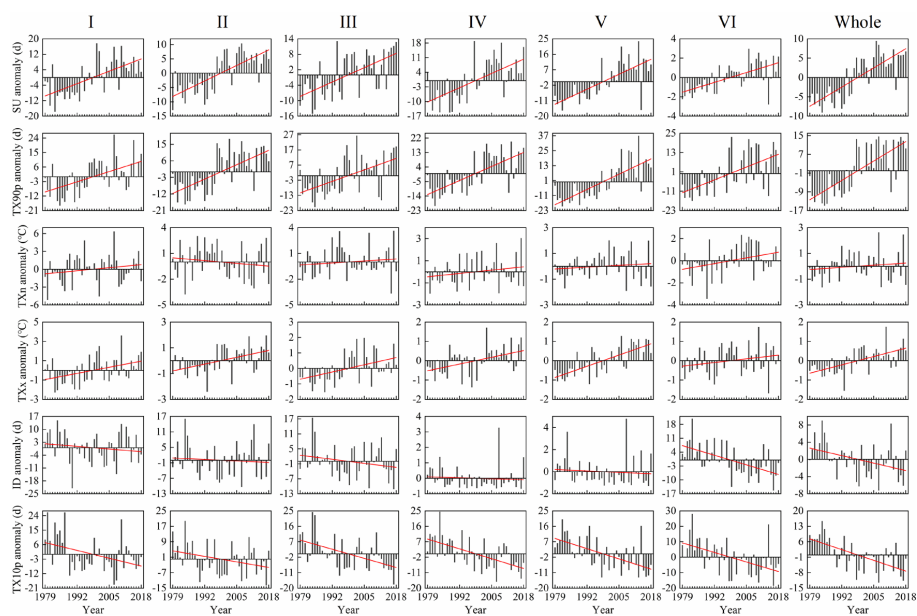
#### 5.3.1 Change of time



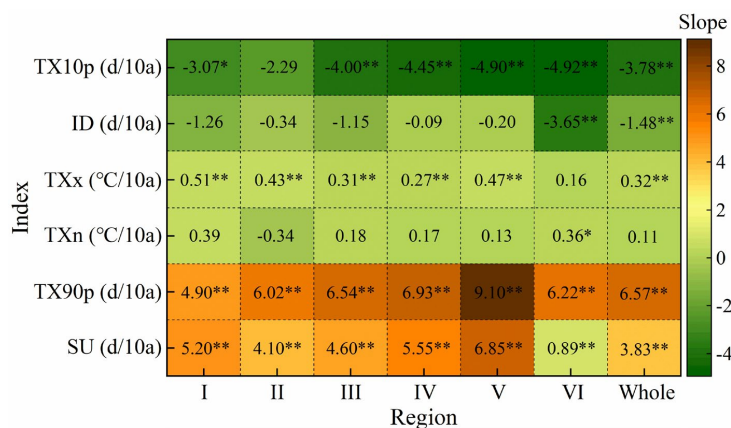
418 We plotted the inter-annual variation of extreme temperature indices anomalies in various regions  
419 of China from 1979 to 2018 (Fig. 10), and used Sen's slope estimation and the Mann-Kendall trend  
420 test to calculate statistics on the trend of extreme temperature indices (Fig. 11). The results indicated  
421 that SU, TX90p, TXn and TXx increased at a rate of 3.83d/10a, 6.57d/10a, 0.11°C/10a and  
422 0.32°C/10a, respectively (Fig. 11). Influenced by the strong El Niño in 1997, the SU in all regions  
423 exhibited a consistent upward trend from 1996 to 1997 (Fig. 10). The change rate of SU in all regions  
424 passed the significance test of 0.01, indicating a significant upward trend (Fig. 11). The increasing  
425 trend of TX90p in all regions was also very significant. The decadal average of TX90p in region  
426 III-VI and the whole study area had an increasing trend, while the decadal average of TX90p in  
427 region I and region II increased first and then decreased slightly. The TXn of region II showed a  
428 weak decreasing trend, and the sliding average of the 3-year and 5-year periods also exhibited a  
429 weak fluctuation downward trend. TXn of other regions showed an upward trend in general, and  
430 only region VI had a significant increasing trend ( $P < 0.05$ ) (Fig. 11). Except for region VI, the  
431 change rate of TXx in other regions was higher than that of TXn. The rate of change of TXx  
432 exhibited that the upward trend of region VI was not significant, while all other regions passed the  
433 significance test of 0.01. During 1979-2018, ID and TX10p decreased significantly at the rate of -  
434 1.48d/10a and -3.78d /10a, respectively ( $P < 0.01$ ) (Fig. 11). The ID of all regions exhibited a  
435 downward trend, with region VI and the whole study area showing the most obvious decline, passing  
436 the significance test of 0.01 (Fig. 11). Compared with ID, TX10p decreased more sharply, and the  
437 highest value of TX10p in all regions occurred before 1988 (Fig. 10). The above results indicate  
438 that the frequency of high temperature events in China is on the rise, which is in line with the  
439 expected results of global change. In addition, we also found that the occurrence time of maximum



440 and minimum values of SU, TXn, TXx and ID during 1979-2018 was consistent with previous  
 441 research results (Hong and Ying, 2018), which further proved the correctness of the  $T_{max}$  dataset  
 442 constructed by us, indicating that built data can be used to analyze the spatial-temporal changes of  
 443 high temperature in China.



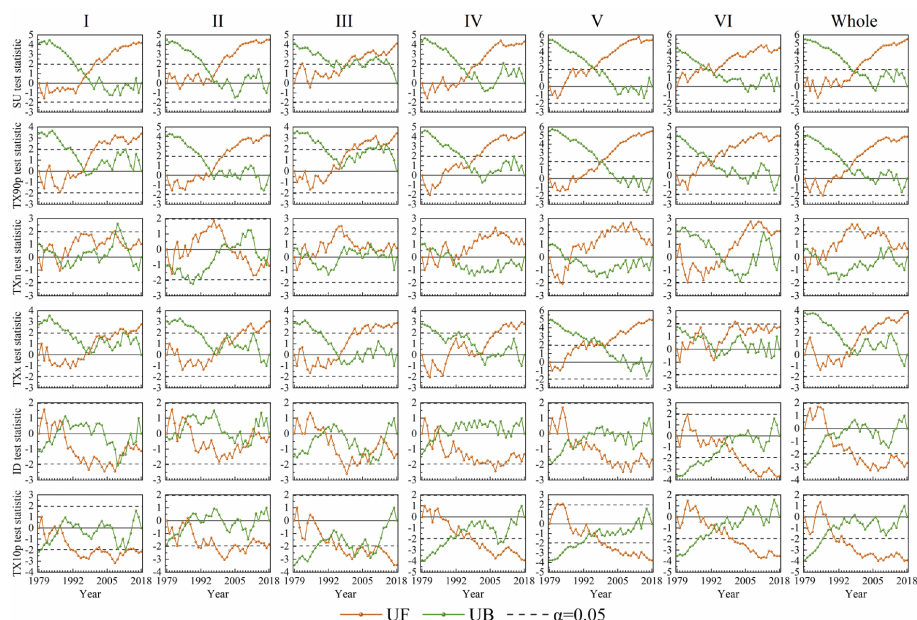
444  
 445 **Figure 10.** Inter-annual trend of extreme temperature indices anomalies in different regions of China during 1979-  
 446 2018.



447  
 448 **Figure 11.** Variation trend of extreme temperature indices in different regions of China from 1979 to 2018. (\*  
 449 significant at the 0.05 level, \*\* significant at the 0.01 level.)



450 In order to analyze the variation rules of extreme temperature indices in China from 1979 to  
451 2018, the Mann-Kendall mutation test was applied to test the mutation characteristics of six extreme  
452 temperature indices at the significance level of 0.05. The results are shown in Fig. 12. During 1979-  
453 2018, all extreme temperature indices had abrupt changes, and 40% of the years where the abrupt  
454 changes occurred were El Niño years, while 46.7% were La Niña years. As can be seen from the  
455 intersection of the UF and UB curves, the SU of region III, V and VI had significant mutation in  
456 2003, 1996 and 1990, respectively, while the other regions had no significant mutation in the whole  
457 period of 1979-2018. TX90p in each region exhibited an overall trend of decreasing first and then  
458 increasing. TX90p in region III was significantly mutated in 2011 and 2013, but the two mutations  
459 did not have much influence on the trend of TX90p. The TXn of region V showed a trend of first  
460 decreasing and then increasing, in contrast with the other regions, which all experienced a process  
461 of increasing and decreasing many times. After mutation in region II in 2003, TXn turned from an  
462 upward trend to a downward trend. Since the UF curve did not exceed the significance level, the  
463 downward trend was not obvious. The TXx of region V exhibited a decreasing trend from 1979 to  
464 1984 but was not significant. After 1984, the TXx kept rising. The UF and UB curves intersected in  
465 1999 and were outside the significance line at the level of 0.05, indicating that the TXx of region V  
466 had a significant mutation in 1999. The ID of the whole study area and its six sub-regions tended to  
467 increase first and then decrease, but the upward trend was not significant. Except for region II, ID  
468 of other regions all showed a significant downward trend. There was a long period of decline in  
469 TX10p in all regions, and the UF value in region II was positive only in 1987. TX10p in region III-  
470 VI and the whole study area has been in a state of significant decline since 1996, 1997, 1998, 2000  
471 and 1993, respectively.



472

473 **Figure 12.** MK abrupt change detection for the extreme temperature indices in different regions of China during  
474 1979–2018.

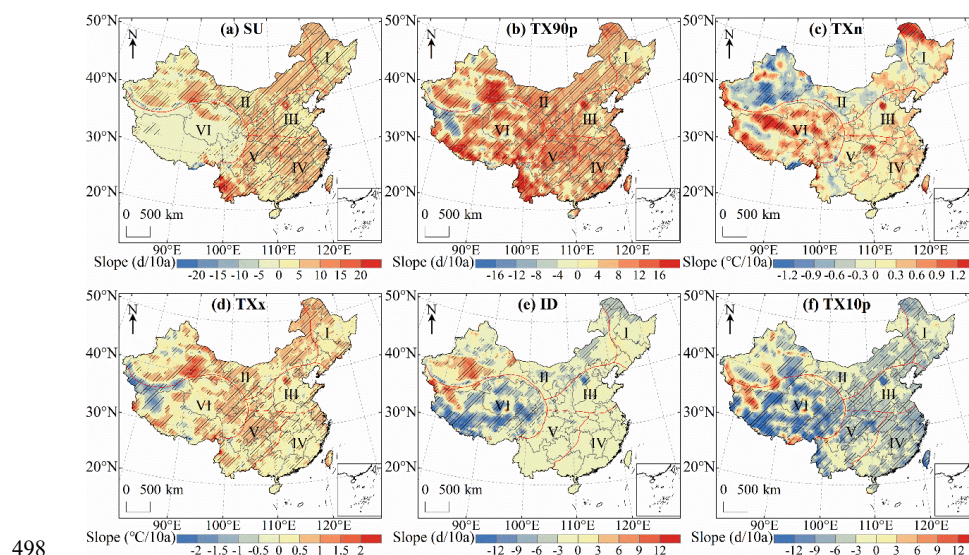
### 475 5.3.2 Spatial change

476 The spatial distribution of the extreme temperature indices trends in China during 1979–2018 is  
477 shown in Fig. 13 (a–f), while the area percentage of the increasing and decreasing trend of extreme  
478 temperature indices in each region is shown in Fig. 14 (a–f). For SU, TX90p, TXn and TXx, the area  
479 with rising trend is larger than the area with declining trend. The change of SU in most regions of  
480 China passed the significance test of 0.05, and the areas with significant increase accounted for 63.3%  
481 of the whole study area (Fig. 14a). The regions with no significant change in SU are mainly  
482 distributed in region VI (Fig. 13a). There are few days in a year when  $T_{\max}$  exceeds 25°C in region  
483 VI, and  $T_{\max}$  in some regions is even lower than 25°C throughout the year, so the change range of  
484 SU is small. The areas with a downward trend of TX90p were mainly distributed in southern  
485 Xinjiang and northern Tibet (Fig. 13b). TX90p increased significantly in 75% of regions in China

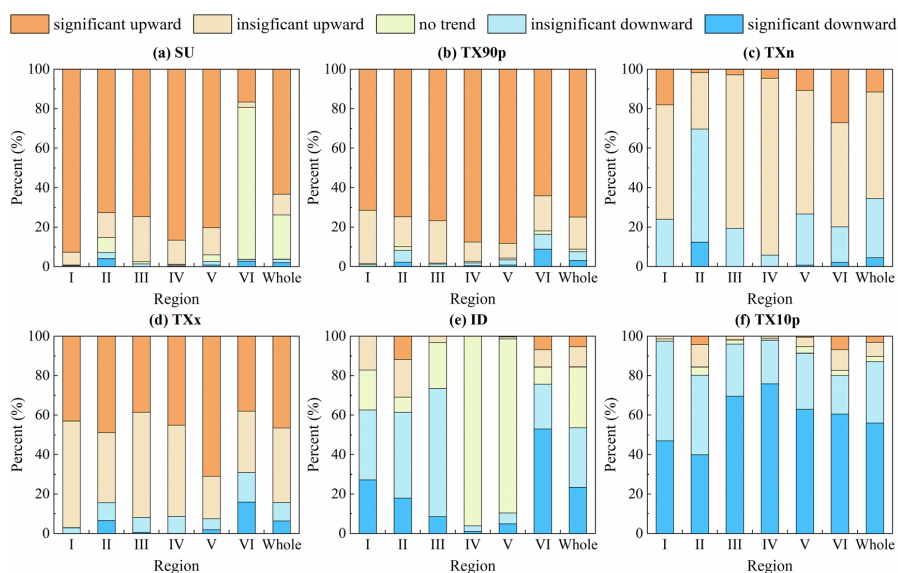




486 (P <0.05), and the area percentage of TX90p significantly increased in region V was the largest  
487 among the six regions (Fig. 14b). The trend of TXn change in most regions of China was not  
488 significant, and the significant decrease was mainly concentrated in region II and region VI (Fig.  
489 13c). While other regions were dominated by increasing trend of the TXn, 69.7% of regions in  
490 region II showed a downward trend (Fig. 14c). For TXx, its upward trend was slightly stronger than  
491 TXn, and the region with the highest change rate was located in western China (Fig. 13d). The  
492 regions with significantly decreased ID were mainly distributed in region VI (Fig. 13e). 75.7% of  
493 the regions had a declining ID, and 53% of the regions passed the significance test (Fig. 14e). As  
494 far as TX10p is concerned, its cooling trend was much stronger than that of ID, and the areas of  
495 significant decline were widely distributed through all regions of China (Fig. 13f). The area with a  
496 significant decrease in region IV accounted for 75.9% of the region, which was the largest among  
497 the six regions (Fig. 14f).



498  
499 **Figure 13.** Spatial distribution of trends in extreme temperature indices over China during 1979-2018. The shaded  
500 areas indicate trends that are statistically significant at the 0.05 level.



501  
 502 **Figure 14.** Area percentage of the trend of extreme temperature indices in different regions of China during 1979-  
 503 2018

## 504 6 Discussion

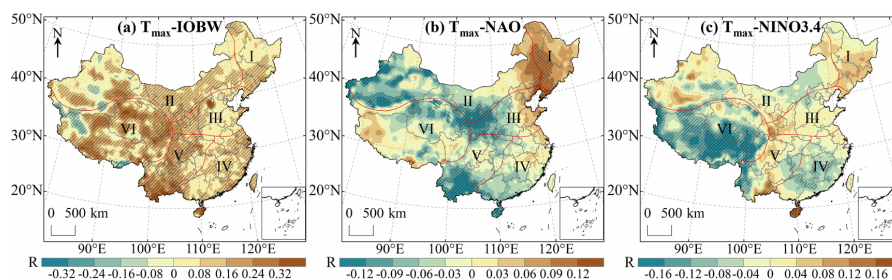
### 505 6.1 The influence of ocean climate modalities on $T_{max}$

506 The correlation between  $T_{max}$  anomalies and three climate modal indices in China during 1979-2018  
 507 is shown in Fig. 15 (a-c). The results show that there is a significant positive correlation between  
 508  $T_{max}$  and IOBW in 54.18% of the regions in China, which indicates that the warming of the Indian  
 509 Ocean will lead to the warming trend of  $T_{max}$  in these regions.  $T_{max}$  had a moderate positive  
 510 correlation ( $0.4 < R < 0.6$ ,  $P < 0.01$ ) with IOBW in southern Yunnan and eastern Hainan. There were  
 511 few areas with significant negative correlation between  $T_{max}$  and IOBW, only accounting for 3.28%  
 512 of regions in China, mainly concentrated in western China, which indicated that the warming Indian  
 513 Ocean will lead to the decreasing trend of  $T_{max}$  in these areas (Fig. 15a).  $T_{max}$  and NAO had a  
 514 significant positive correlation in northeast China, but the correlation was very weak ( $R < 0.2$ ). The  
 515 percentage of  $T_{max}$  anomaly value negatively correlated with NAO (16.55%) was higher than that





516 of NAO positively correlated (5.27%), mainly distributed in the west and south of region II, west of  
517 region III, south of region IV and V, and northeast of region VI. This indicated that the positive  
518 phase of NAO led to the decrease of  $T_{\max}$  in these regions (Fig. 15b).  $T_{\max}$  was significantly  
519 positively correlated with NINO3.4 in southern China, central Xinjiang and southern Gansu,  
520 indicating that El Niño events will lead to higher temperatures in these regions. In western China  
521 and the middle part of region IV,  $T_{\max}$  was significantly negatively correlated with NINO3.4,  
522 indicating that El Niño events will lead to cooling phenomena in these regions (Fig. 15c).



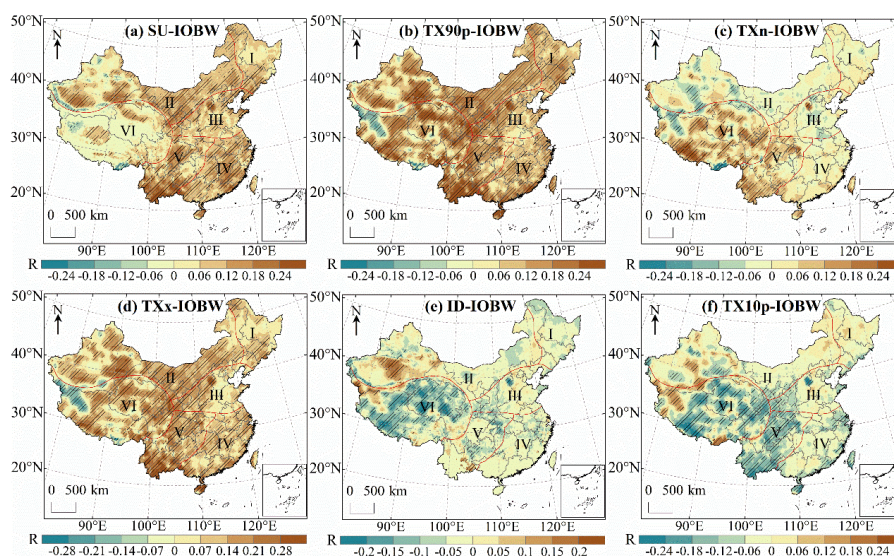
523 **Figure 15.** Correlation analysis between  $T_{\max}$  and IOBW (a), NAO (b) and NINO3.4 (c) in China during 1979-  
524 2018. The shaded areas indicate trends that are statistically significant at the 0.05 level.

## 526 6.2 The influence of ocean climate mode on extreme temperature indices

527 Fig. 16 (a-f) indicates the spatial distribution of the correlation between extreme temperature indices  
528 anomalies and IOBW in China during 1979-2018. It can be seen that SU, TX90p, TXn and TXx  
529 over most of China are positively correlated with the IOBW. The region with significant positive  
530 correlation between the SU and IOBW accounted for 42.67% of the whole study area, which  
531 indicated that a warming Indian Ocean would lead to the number of days over 25°C in these regions  
532 to increase. Significant negative correlations were found in northwest and southeast Tibet and the  
533 mountainous regions of southern Xinjiang (Fig. 16a). The area with the largest correlation  
534 coefficient is in the northeast of Hainan (R=0.48). The significant negative correlation between  
535 TX90p and IOBW was mainly distributed in region VI, but the negative correlation was not strong



536 ( $|R| < 0.4$ ) (Fig. 16b). The correlation coefficient between TX<sub>n</sub> and IOBW ranged from -0.34 to  
537 0.34, and the regions with significant positive correlation accounted for 16.65% of the whole study  
538 area. TX<sub>n</sub> and IOBW were significantly negatively correlated mainly in western China (Fig. 16c).  
539 Compared with TX<sub>n</sub>, the regions with significant correlation between TX<sub>x</sub> and IOBW were more  
540 widely distributed in China, among which the correlation coefficients in southern Yunnan and  
541 eastern Hainan were moderately positive ( $0.4 < R < 0.6$ ) (Fig. 16d). ID and TX<sub>10p</sub> were negatively  
542 correlated with IOBW in most of China. The regions with significant negative correlation between  
543 ID and IOBW were mainly distributed in region VI, and the regions with significant positive  
544 correlation were mainly distributed in the west of region II (Fig. 16e). TX<sub>10p</sub> has a significant  
545 negative correlation with IOBW in more areas than ID, and the significant positive correlation was  
546 mainly located in western China (Fig. 16f).



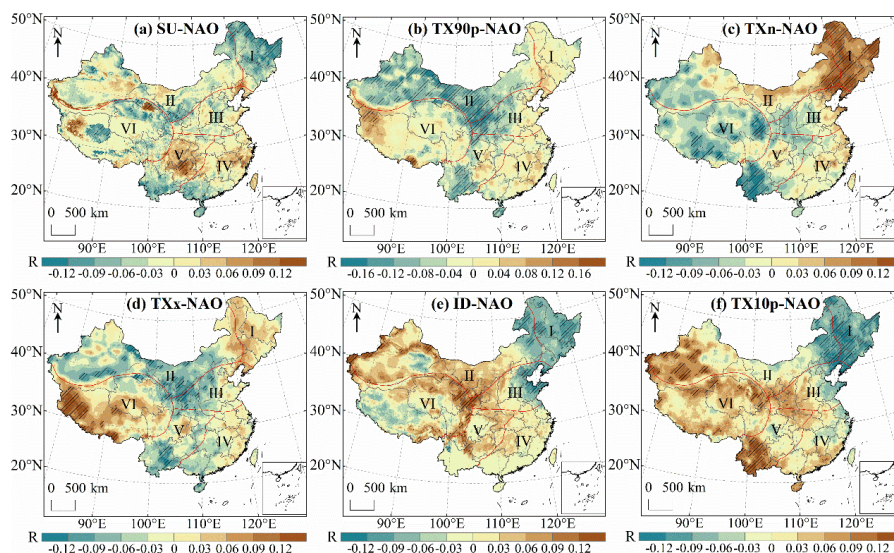
547  
548 **Figure 16.** Correlation analysis between extreme temperature indices and IOBW in China during 1979-2018. The  
549 shaded areas indicate trends that are statistically significant at the 0.05 level.



550 The influence of NAO on the extreme temperature indices is shown in Fig.17 (a-f). SU, TX90p,  
551 TXx and TXn were negatively correlated with the NAO more than they were positively correlated  
552 with NAO, indicating that the positive phase of NAO would lead to the decline of SU, TX90p, TXx  
553 and TXn over most of China. SU and NAO had a significant positive correlation in southern  
554 Xinjiang, western Tibet, northern Qinghai and northern Guizhou, but the correlation was very weak  
555 ( $R < 0.2$ ). There was no significant correlation between SU and NAO in southern Qinghai, which  
556 was consistent with previous observations (Ding et al., 2018). The region with the strongest negative  
557 correlation between SU and NAO was located in Tibet ( $R = -0.18$ ) (Fig. 17a). TX90p had a weak  
558 negative correlation with NAO in eastern Xinjiang ( $R = -0.22$ ,  $P < 0.01$ ). TX90p was significantly  
559 positively correlated with NAO in the west and south of region VI, but the correlation was extremely  
560 weak (Fig. 17b). Shi et al. (2019) indicated that more regions had a significant positive correlation  
561 between TXn and NAO in China than had a significant negative correlation, which was consistent  
562 with our results. The areas of TXn had a significant positive correlation with NAO were mainly  
563 distributed in northeast China, while the regions with significant negative correlation were mainly  
564 located in central Tibet, eastern Qinghai and Yunnan (Fig. 17c). The correlation coefficient between  
565 TXx and NAO varied from -0.16 to 0.21. The regions with significant positive correlation between  
566 TXx and NAO were mainly located in Tibet, and the region with the strongest correlation was  
567 located in southern Tibet (Fig. 17d). The areas of ID was significantly positively correlated with  
568 NAO accounted for 5.86% of the whole study area, and the strongest correlation was found in  
569 western Xinjiang ( $R = 0.23$ ). The regions with significant negative correlation between ID and NAO  
570 were mainly distributed in eastern and northeastern China (Fig. 17e). Sun et al. (2016) found a very  
571 weak positive correlation between TX10p and NAO in the Loess Plateau, which was consistent with



572 our results. The regions with a significant negative correlation were mainly concentrated in  
573 northeastern China (Fig. 17f).



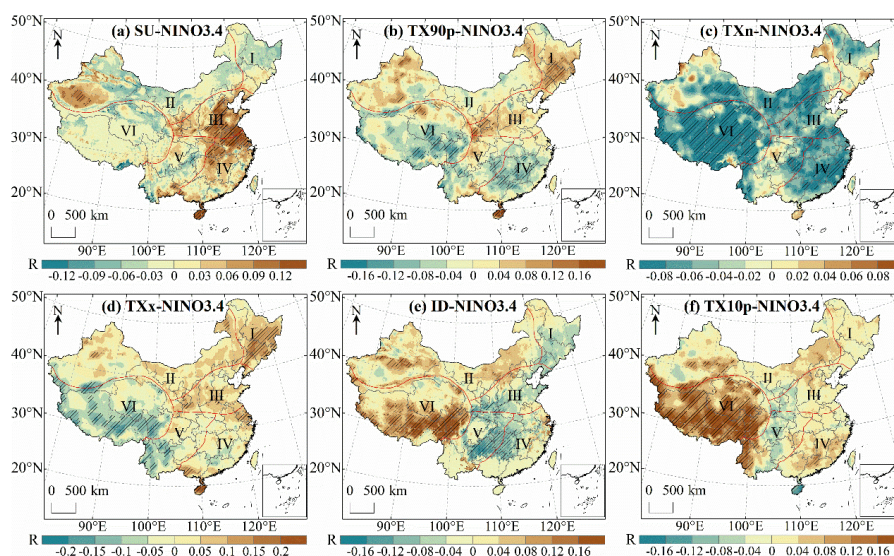
574  
575 **Figure 17.** Correlation analysis between extreme temperature indices and NAO in China during 1979-2018. The  
576 shaded areas indicate trends that are statistically significant at the 0.05 level.

577 Fig.18 (a-f) shows the correlation between NINO3.4 and extreme temperature indices. The  
578 regions with significant positive correlation between SU and NINO3.4 were mainly distributed in  
579 eastern China, indicating that the events of El Niño would lead to an upward trend of SU in these  
580 regions. There were few regions with significant negative correlation between SU and NINO3.4,  
581 only accounting for 1.15% of the entire research area, mainly distributed in southeast Tibet and  
582 southwest Yunnan (Fig. 18a). The correlation coefficient between TX90p and NINO3.4 was -0.19-  
583 0.26. The areas of TX90p had a significant negative correlation with NINO3.4 were mainly  
584 distributed in region IV and VI (Fig. 18b). There was a significant negative correlation between  
585 TXn and NINO3.4 in 24.59% of regions, and the region with the strongest negative correlation was  
586 located in Tibet ( $R=-0.25$ ). TXn was positively correlated with NINO3.4 in only 10.46% of regions





587 in China, and the region with the largest correlation coefficient was northwest Xinjiang ( $R=0.11$ )  
588 (Fig. 18c). There was a weak positive correlation between TXx and NINO3.4 in southern  
589 Guangdong and northern Hainan ( $0.2 < R < 0.4$ ). The regions of TXx was significantly negatively  
590 correlated with NINO3.4 were mainly distributed in the south of region V and region VI (Fig. 18d).  
591 The significant negative correlation between ID and NINO3.4 was mainly concentrated in southern  
592 China. The areas with significant positive correlation were mainly distributed in the western region  
593 II and southern region VI, and the region with the strongest correlation was located in the western  
594 Sichuan ( $R=0.31$ ) (Fig. 18e). TX10p in most regions of regional VI was significantly affected by  
595 NINO3.4, and the significant positive correlation area accounted for 69.31% of the whole region VI.  
596 TX10p was significantly negatively correlated with NINO3.4 in only 0.65% of regions in China,  
597 mainly distributed in Hainan and southern Gansu (Fig. 18f).



598  
599 **Figure 18.** Correlation analysis between extreme temperature indices and NINO3.4 in China during 1979-2018.

600 The shaded areas indicate trends that are statistically significant at the 0.05 level.

## 601 7 Conclusions



602 The global temperature continues to rise and extreme weather events continue to increase. It is great  
603 significance to study regional high temperature changes. In order to obtain the key parameters of  
604 high temperature spatial-temporal variation analysis, this study proposed a daily  $T_{\max}$  estimation  
605 frame based on the near-surface  $T_a$  grid data and  $T_a$  diurnal variation model to build a  $T_{\max}$  dataset  
606 in China from 1979 to 2018. Validation of  $T_{\max}$  estimation data in six natural regions indicated that  
607 the RMSE of each region was between 2.38-2.94°C, the MAE was between 1.88-2.45°C, and  $R^2$   
608 was between 0.95-0.99. After using the regression model to calibrate the dataset, the accuracy of  
609 the estimated  $T_{\max}$  has been significantly improved. The RMSE of the  $T_{\max}$  after calibration reduced  
610 to 1.14-1.81°C, and the MAE reduced to 0.84-1.38°C, and the  $R^2$  increased to 0.97-0.99.

611 This dataset was used to study the spatial-temporal variation characteristics of  $T_{\max}$  and the  
612 corresponding influencing factors in China, and to discuss the correlation between  $T_{\max}$ , extreme  
613 temperature indices and ocean climate modal indices.  $T_{\max}$  in all regions of China exhibited an  
614 upward trend from 1979 to 2018, with the largest rise in region V and the smallest rise in region I.  
615 In spring,  $T_{\max}$  in China increased significantly in most regions, and the region III is with the fastest  
616 rising speed. In winter,  $T_{\max}$  in China had the least significant rise, and the region II was with the  
617 slowest rise rate. SU, TX90p and TXx in all regions showed an upward trend. Except for region II,  
618 TXn in other regions also exhibited an upward trend, while ID and TX10p in all regions showed a  
619 downward trend. All extreme temperature indices had abrupt changes during 1979-2018, and most  
620 of the abrupt changes occurred in El Niño or La Niña years. The region with the largest increase of  
621 SU, TX90p and TXx and the region with the largest decrease of TX10p were located in the western  
622 Yunnan. The correlation analysis between  $T_{\max}$  and extreme temperature indices and ocean climate  
623 modal indices indicated that the increase of the IOBW usually led to the increase of  $T_{\max}$ , SU, TX90p,



624 TXn and TXx and the decrease of ID and TX10p. NAO had the opposite relationships. In most  
625 regions of China,  $T_{max}$ , SU, TX90p and TXn were negatively correlated with NINO.3.4, while TXx,  
626 ID and TX10p were positively correlated with NINO.3.4.

627 The analysis of regional high temperature temporal and spatial changes shows that the  
628 temperature changes in different regions of China are inconsistent, and the mechanism that affects  
629 the temperature rise is different in different regions, and some regions are highly correlated with  
630 ocean temperature changes. In order to strengthen environmental protection and control temperature  
631 rise, and formulate reasonable carbon emission reduction measures, we need further research in the  
632 future.

633

634 *Data availability.* CMFD is available from the National Qinghai-Tibet Plateau Science Data Center  
635 (<https://data.tpdc.ac.cn/>). ERA5 data can be obtained from the ECMWF ERA5 data website  
636 (<https://cds.climate.copernicus.eu/>). Meteorological station data is available by CMA National  
637 Meteorological Information Center (<http://data.cma.cn/>). IOBW index can be accessed at the  
638 National Climate Center of CMA (<http://cmdp.ncc-cma.net/cn/index.htm>), and NAO index and  
639 NINO3.4 index are from the National Oceanic and Atmospheric Administration of the United States  
640 (<https://psl.noaa.gov/data/climateindices/list/>).

641

642 *Author contributions.* PW and KM proposed the goals and aims of the research. FM provided  
643 supervision and scientific guidance for the research. PW and SF built the dataset production model.  
644 PW wrote the paper. KM, ZQ, SMB, and MA revised the final manuscript.

645

646 *Competing interests.* The authors declare no conflicts of interest.



647

648 *Acknowledgements.* The authors thank the China Meteorological Administration for providing  
649 IOBW index and the ground measurements data, the Institute of Tibetan Plateau Research, Chinese  
650 Academy of Sciences for providing CMFD dataset, and the NASA Earth Observing System Data  
651 and Information System for providing the DEM data. We also thank the National Oceanic and  
652 Atmospheric Administration of the United States for providing the ocean climate modal indices and  
653 the ECMWF for providing the climate reanalysis data.

654

655 *Financial support.* This work is supported by the National Key Research and Development Program  
656 of China (2019YFE0127600), National Natural Science Foundation of China (41771406), the  
657 Fundamental Research Funds for Central Nonprofit Scientific Institution (1610132020014) and the  
658 Open Fund of the State Key Laboratory of Remote Sensing Science (grant no. OFSLRSS201910).

659

## 660 **References**

- 661 Abdullah, A. M., Ismail, M., Yuen, F. S., Abdullah, S., and Elhadi, R. E.: The Relationship between  
662 Daily Maximum Temperature and Daily Maximum Ground Level Ozone Concentration, Polish  
663 Journal of Environmental Studies, 26, 517-523, <https://doi.org/10.15244/pjoes/65366>, 2017.
- 664 Basu, R.: High ambient temperature and mortality: a review of epidemiologic studies from 2001 to 2008,  
665 Environmental health, 8, 40, <https://doi.org/10.1186/1476-069X-8-40>, 2009.
- 666 Benali, A., Carvalho, A. C., Nunes, J. P., Carvalhais, N., and Santos, A.: Estimating air surface  
667 temperature in Portugal using MODIS LST data, Remote Sensing of Environment, 124, 108-121,  
668 <https://doi.org/10.1016/j.rse.2012.04.024>, 2012.
- 669 Cao, M. M., Mao, K. B., Shen, X. Y., Xu, T. R., Yan, Y. B., and Yuan, Z. J.: Monitoring the Spatial and  
670 Temporal Variations in The Water Surface and Floating Algal Bloom Areas in Dongting Lake Using  
671 a Long-Term MODIS Image Time Series, Remote Sensing, 12, 3622,  
672 <https://doi.org/10.3390/rs12213622>, 2020.
- 673 Ding, Z. Y., Wang, Y. Y., and Lu, R. J.: An analysis of changes in temperature extremes in the Three  
674 River Headwaters region of the Tibetan Plateau during 1961-2016, Atmospheric Research, 209, 103-  
675 114, <https://doi.org/10.1016/j.atmosres.2018.04.003>, 2018.
- 676 Du, Q. Q., Zhang, M. J., Wang, S. J., Che, C. W., Ma, R., and Ma, Z. Z.: Changes in air temperature over  
677 China in response to the recent global warming hiatus, Journal of Geographical Sciences, 29, 496-516,  
678 <https://doi.org/10.1007/s11442-019-1612-3>, 2019.





- 679 Ephrath, J. E., Goudriaan, J., and Marani, A.: Modelling diurnal patterns of air temperature, radiation  
680 wind speed and relative humidity by equations from daily characteristics, *Agricultural Systems*, 51,  
681 377-393, [https://doi.org/10.1016/0308-521X\(95\)00068-G](https://doi.org/10.1016/0308-521X(95)00068-G), 1996.
- 682 Evrendilek, F., Karakaya, N., Gungor, K., and Aslan, G.: Satellite-based and mesoscale regression  
683 modeling of monthly air and soil temperatures over complex terrain in Turkey, *Expert Systems with*  
684 *Applications*, 39, 2059-2066, <https://doi.org/10.1016/j.eswa.2011.08.023>, 2012.
- 685 Fabiola, F. P. and Mario, L. S.: Simple air temperature estimation method from MODIS satellite images  
686 on a regional scale, *Chilean Journal of Agricultural Research*, 70, 436-445,  
687 <https://doi.org/10.4067/S0718-58392010000300011>, 2010.
- 688 Gasparrini, A. and Armstrong, B.: The impact of heat waves on mortality, *Epidemiology*, 22, 68-73,  
689 <https://doi.org/10.1097/EDE.0b013e3181fdcd99>, 2011.
- 690 Gu, H. H., Yu, Z. B., Peltier, W. R., and Wang, X. Y.: Sensitivity studies and comprehensive evaluation  
691 of RegCM4. 6.1 high-resolution climate simulations over the Tibetan Plateau, *Climate Dynamics*, 54,  
692 3781-3801, <https://doi.org/10.1007/s00382-020-05205-6>, 2020.
- 693 Guan, Y. H., Zhang, X. C., Zheng, F. L., and Wang, B.: Trends and variability of daily temperature  
694 extremes during 1960–2012 in the Yangtze River Basin, China, *Global and Planetary Change*, 124,  
695 79-94, <https://doi.org/10.1016/j.gloplacha.2014.11.008>, 2015.
- 696 He, J., Yang, K., Tang, W. J., Lu, H., Qin, J., Chen, Y. Y., and Li, X.: The first high-resolution  
697 meteorological forcing dataset for land process studies over China, *Scientific Data* 7, 1-11,  
698 <https://doi.org/10.1038/s41597-020-0369-y>, 2020.
- 699 Hoffmann, L., Günther, G., Li, D., Stein, O., Wu, X., Griessbach, S., Heng, Y., Konopka, P., Müller, R.,  
700 Vogel, B., and Wright, J. S.: From ERA-Interim to ERA5: the considerable impact of ECMWF's next-  
701 generation reanalysis on Lagrangian transport simulations, *Atmospheric Chemistry and Physics*, 19,  
702 3097-3124, <https://doi.org/10.5194/acp-19-3097-2019>, 2019.
- 703 Hong, Y. and Ying, S.: Characteristics of extreme temperature and precipitation in China in 2017 based  
704 on ETCCDI indices, *Advances in Climate Change Research*, 9, 218-226,  
705 <https://doi.org/10.1016/j.accres.2019.01.001>, 2018.
- 706 Johnson, M. E. and Fitzpatrick, E. A.: A comparison of two methods of estimating a mean diurnal  
707 temperature curve during the daylight hours, *Archiv für Meteorologie, Geophysik und*  
708 *Bioklimatologie, Serie B*, 25, 251-263, <https://doi.org/10.1007/BF02243056>, 1977.
- 709 Khan, N., Shahid, S., Ismail, T. B., and Wang, X. J.: Spatial distribution of unidirectional trends in  
710 temperature and temperature extremes in Pakistan, *Theoretical and Applied Climatology*, 136, 899-  
711 913, <https://doi.org/10.1007/s00704-018-2520-7>, 2018.
- 712 Kleinert, F., Leufen, L. H., and Schultz, M. G.: IntelliO3-ts v1. 0: a neural network approach to predict  
713 near-surface ozone concentrations in Germany, *Geoscientific Model Development*, 14, 1-25,  
714 <https://doi.org/10.5194/gmd-14-1-2021>, 2021.
- 715 Li, L. C., Yao, N., Li, Y., Liu, D. L., Wang, B., and Ayantobo, O. O.: Future projections of extreme  
716 temperature events in different sub-regions of China, *Atmospheric Research*, 217, 150-164,  
717 <https://doi.org/10.1016/j.atmosres.2018.10.019>, 2019a.
- 718 Li, Q. X., Yang, S., Xu, W. H., Wang, X. L., Jones, P., Parker, D., Zhou, L. M., Feng, Y., and Gao, Y.:  
719 China experiencing the recent warming hiatus, *Geophysical Research Letters*, 42, 889-898,  
720 <https://doi.org/10.1002/2014GL062773>, 2015.



- 721 Li, Y. L., Han, W. Q., Zhang, L., and Wang, F.: Decadal SST variability in the southeast Indian Ocean  
722 and its impact on regional climate, *Journal of Climate*, 32, 6299-6318, [https://doi.org/10.1175/JCLI-  
D-19-0180.1](https://doi.org/10.1175/JCLI-<br/>723 D-19-0180.1), 2019b.
- 724 Lin, S. P., Moore, N. J., Messina, J. P., DeVisser, M. H., and Wu, J. P.: Evaluation of estimating daily  
725 maximum and minimum air temperature with MODIS data in east Africa, *International Journal of  
726 Applied Earth Observation and Geoinformation*, 18, 128-140,  
727 <https://doi.org/10.1016/j.jag.2012.01.004>, 2012.
- 728 Luan, J. K., Zhang, Y. Q., Tian, J., Meresa, H. K., and Liu, D. F.: Coal mining impacts on catchment  
729 runoff, *Journal of Hydrology*, 589, 125101, <https://doi.org/10.1016/j.jhydrol.2020.125101>, 2020.
- 730 McGree, S., Herold, N., Alexander, L., Schreider, S., Kuleshov, Y., Ene, E., Finaulahi, S., Inape, K.,  
731 Mackenzie, B., Malala, H., Ngari, A., Prakash, B., and Tahani, L.: Recent changes in mean and  
732 extreme temperature and precipitation in the Western Pacific Islands, *Journal of Climate*, 32, 4919-  
733 4941, <https://doi.org/10.1175/JCLI-D-18-0748.1> 2019.
- 734 Ninyerola, M., Pons, X., and Roure, J. M.: A methodological approach of climatological modelling of  
735 air temperature and precipitation through GIS techniques, *International Journal of Climatology*, 20,  
736 1823-1841, [https://doi.org/10.1002/1097-0088\(20001130\)20:14<1823::AID-JOC566>3.0.CO;2-B](https://doi.org/10.1002/1097-0088(20001130)20:14<1823::AID-JOC566>3.0.CO;2-B),  
737 2000.
- 738 Parton, W. J. and Logan, J. A.: A model for diurnal variation in soil and air temperature, *Agricultural  
739 Meteorology*, 23, 205-216, [https://doi.org/10.1016/0002-1571\(81\)90105-9](https://doi.org/10.1016/0002-1571(81)90105-9), 1981.
- 740 Poudel, A., Cuo, L., Ding, J., and Gyawali, A. R.: Spatio - temporal variability of the annual and monthly  
741 extreme temperature indices in Nepal, *International Journal of Climatology*, 40, 4956-4977,  
742 <https://doi.org/10.1002/joc.6499>, 2020.
- 743 Ruml, M., Gregorić, E., Vujadinović, M., Radovanović, S., Matović, G., Vuković, A., Počuča, V., and  
744 Stojičić, D.: Observed changes of temperature extremes in Serbia over the period 1961 – 2010,  
745 *Atmospheric Research*, 183, 26-41, <https://doi.org/10.1016/j.atmosres.2016.08.013>, 2017.
- 746 Salman, S. A., Shahid, S., Ismail, T., Chung, E.-S., and Al-Abadi, A. M.: Long-term trends in daily  
747 temperature extremes in Iraq, *Atmospheric Research*, 198, 97-107,  
748 <https://doi.org/10.1016/j.atmosres.2017.08.011>, 2017.
- 749 Sathaye, J. A., Dale, L. L., Larsen, P. H., Fitts, G. A., Koy, K., Lewis, S. M., and de Lucena, A. F. P.:  
750 Estimating impacts of warming temperatures on California's electricity system, *Global Environmental  
751 Change*, 23, 499-511, <https://doi.org/10.1016/j.gloenvcha.2012.12.005>, 2013.
- 752 Seenu, P. Z. and Jayakumar, K. V.: Comparative study of innovative trend analysis technique with Mann-  
753 Kendall tests for extreme rainfall, *Arabian Journal of Geosciences*, 14, 1-15,  
754 <https://doi.org/10.1007/s12517-021-06906-w>, 2021.
- 755 Sehra, S. T., Saliccioli, J. D., Wiebe, D. J., Fundin, S., and Baker, J. F.: Maximum daily temperature,  
756 precipitation, ultraviolet light, and rates of transmission of severe acute respiratory syndrome  
757 coronavirus 2 in the United States, *Clinical Infectious Diseases*, 71, 2482-2487,  
758 <https://doi.org/10.1093/cid/ciaa681>, 2020.
- 759 Sen, P. K.: Estimates of the regression coefficient based on Kendall's tau, *Journal of the American  
760 Statistical Association*, 63, 1379-1389, <https://doi.org/10.2307/2285891> 1968.
- 761 Shen, S. H. and Leptoukh, G. G.: Estimation of surface air temperature over central and eastern Eurasia  
762 from MODIS land surface temperature, *Environmental Research Letters*, 6, 045206,  
763 <https://doi.org/10.1088/1748-9326/6/4/045206> 2011.



- 764 Shi, J., Cui, L. L., Wang, J. B., Du, H. Q., and Wen, K. M.: Changes in the temperature and precipitation  
765 extremes in China during 1961–2015, *Quaternary International*, 527, 64–78,  
766 <https://doi.org/10.1016/j.quaint.2018.08.008>, 2019.
- 767 Sun, W. Y., Mu, X. M., Song, X. Y., Wu, D., Cheng, A. F., and Qiu, B.: Changes in extreme temperature  
768 and precipitation events in the Loess Plateau (China) during 1960–2013 under global warming,  
769 *Atmospheric Research*, 168, 33–48, <http://dx.doi.org/10.1016/j.atmosres.2015.09.001>, 2016.
- 770 Sun, Y. J., Wang, J. F., Zhang, R. H., Gillies, R. R., Xue, Y., and Bo, Y. C.: Air temperature retrieval  
771 from remote sensing data based on thermodynamics, *Theoretical and Applied Climatology*, 80, 37–48,  
772 <https://doi.org/10.1007/s00704-004-0079-y>, 2005.
- 773 Tan, M. L., Samat, N., Chan, N. W., Lee, A. J., and Li, C.: Analysis of Precipitation and Temperature  
774 Extremes over the Muda River Basin, Malaysia, *Water*, 11, 1–16, <https://doi.org/10.3390/w11020283>,  
775 2019.
- 776 Tong, S. Q., Li, X. Q., Zhang, J. Q., Bao, Y. H., Bao, Y. B., Na, L., and Si, A. L.: Spatial and temporal  
777 variability in extreme temperature and precipitation events in Inner Mongolia (China) during 1960–  
778 2017, *Science of the Total Environment*, 649, 75–89, <https://doi.org/10.1016/j.scitotenv.2018.08.262>,  
779 2019.
- 780 Urraca, R., Huld, T., Gracia-Amillo, A., Martinez-de-Pison, F. J., Kaspar, F., and Sanz-Garcia, A.:  
781 Evaluation of global horizontal irradiance estimates from ERA5 and COSMO-REA6 reanalyses using  
782 ground and satellite-based data, *Solar Energy*, 164, 339–354,  
783 <https://doi.org/10.1016/j.solener.2018.02.059>, 2018.
- 784 Wang, X. X., Jiang, D. B., and Lang, X. M.: Extreme temperature and precipitation changes associated  
785 with four degree of global warming above pre - industrial levels, *International Journal of Climatology*,  
786 39, 1822–1838, <https://doi.org/10.1002/joc.5918>, 2019.
- 787 Wang, Y., Peng, D. L., Shen, M. G., Xu, X. Y., Yang, X. H., Huang, W. J., Yu, L., Liu, L. Y., Li, C. J.,  
788 and Li, X. W.: Contrasting Effects of Temperature and Precipitation on Vegetation Greenness along  
789 Elevation Gradients of the Tibetan Plateau, *Remote Sensing*, 12, 2751,  
790 <https://doi.org/10.3390/rs12172751>, 2020.
- 791 Wloczyk, C., Borg, E., Richter, R., and Miegel, K.: Estimation of instantaneous air temperature above  
792 vegetation and soil surfaces from Landsat 7 ETM+ data in northern Germany, *International Journal of*  
793 *Remote Sensing*, 32, 9119–9136, <https://doi.org/10.1080/01431161.2010.550332>, 2011.
- 794 Wu, R. G., Yang, S., Liu, S., Sun, L., Lian, Y., and Gao, Z. T.: Northeast China summer temperature and  
795 north Atlantic SST, *Journal of Geophysical Research*, 116, <https://doi.org/10.1029/2011JD015779>,  
796 2011.
- 797 Yan, Y. B., Mao, K. B., Shen, X. Y., Cao, M. M., Xu, T. R., Guo, Z. H., and Bao, Q.: Evaluation of the  
798 influence of ENSO on tropical vegetation in long time series using a new indicator, *Ecological*  
799 *Indicators*, 129, 107872, <https://doi.org/10.1016/j.ecolind.2021.107872>, 2021.
- 800 Yang, Z. Y., Shen, M. G., Jia, S. G., Guo, L., Yang, W., Wang, C., Chen, X. H., and Chen, J.: Asymmetric  
801 responses of the end of growing season to daily maximum and minimum temperatures on the Tibetan  
802 Plateau, *Journal of Geophysical Research*, 122, 278–287, <https://doi.org/10.1002/2017JD027318>,  
803 2017.
- 804 Yoo, C., Im, J., Park, S., and Quackenbush, L. J.: Estimation of daily maximum and minimum air  
805 temperatures in urban landscapes using MODIS time series satellite data, *ISPRS Journal of*  
806 *Photogrammetry and Remote Sensing*, 137, 149–162, <https://doi.org/10.1016/j.isprsjprs.2018.01.018>,  
807 2018.



- 808 You, Q. L., Kang, S. C., Aguilar, E., Pepin, N., Flügel, W.-A., Yan, Y. P., Xu, Y. W., Zhang, Y. J., and  
809 Huang, J.: Changes in daily climate extremes in China and their connection to the large scale  
810 atmospheric circulation during 1961–2003, *Climate Dynamics*, 36, 2399–2417,  
811 <https://doi.org/10.1007/s00382-009-0735-0>, 2011.
- 812 Zhai, P. M., Yu, R., Guo, Y. J., Li, Q. X., Ren, X. J., Wang, Y. Q., Xu, W. H., Liu, Y. J., and Ding, Y.  
813 H.: The strong El Niño in 2015/2016 and its dominant impacts on global and China's climate, *Acta*  
814 *Meteorologica Sinica*, 74, 309–321. (In Chinese), <https://doi.org/10.11676/qxxb2016.049>, 2016.
- 815 Zhang, H., Da, Y. B., Zhang, X., and Fan, J. L.: The impacts of climate change on coal-fired power plants:  
816 evidence from China, *Energy & Environmental Science*, 14, 4890–4902,  
817 <https://doi.org/10.1039/D1EE01475G>, 2021.
- 818 Zhang, M., Du, S. Q., Wu, Y. J., Wen, J. H., Wang, C. X., Xu, M., and Wu, S. Y.: Spatiotemporal changes  
819 in frequency and intensity of high-temperature events in China during 1961–2014, *Journal of*  
820 *Geographical Sciences*, 27, 1027–1043, <https://doi.org/10.1007/s11442-017-1419-z>, 2017.
- 821 Zhang, P. F., Ren, G. Y., Xu, Y., Wang, X. L. L., Qin, Y., Sun, X. B., and Ren, Y. Y.: Observed changes  
822 in extreme temperature over the global land based on a newly developed station daily dataset, *Journal*  
823 *of Climate*, 32, 8489–8509, <https://doi.org/10.1175/JCLI-D-18-0733.1> 2019.
- 824 Zhao, B., Mao, K. B., Cai, Y. L., Shi, J. C., Li, Z. L., Qin, Z. H., Meng, X. J., Shen, X. Y., and Guo, Z.  
825 H.: A combined Terra and Aqua MODIS land surface temperature and meteorological station data  
826 product for China from 2003 to 2017, *Earth System Science Data*, 12, 2555–2577,  
827 <https://doi.org/10.5194/essd-12-2555-2020>, 2020.
- 828 Zheng, X., Zhu, J. J., and Yan, Q. L.: Monthly air temperatures over Northern China estimated by  
829 integrating MODIS data with GIS techniques, *Journal of Applied Meteorology and Climatology*, 52,  
830 1987–2000, <https://doi.org/10.1175/JAMC-D-12-0264.1> 2013.
- 831 Zhong, K. Y., Zheng, F. L., Wu, H. Y., Qin, C., and Xu, X. M.: Dynamic changes in temperature extremes  
832 and their association with atmospheric circulation patterns in the Songhua River Basin, China,  
833 *Atmospheric Research*, 190, 77–88, <https://doi.org/10.1016/j.atmosres.2017.02.012>, 2017.
- 834 Zhou, B. T., Xu, Y., Wu, J., Dong, S. Y., and Shi, Y.: Changes in temperature and precipitation extreme  
835 indices over China: Analysis of a high - resolution grid dataset, *International Journal of Climatology*,  
836 36, 1051–1066, <https://doi.org/10.1002/joc.4400>, 2016.
- 837 Zhu, S. Y., Zhou, C. X., Zhang, G. X., Zhang, H. L., and Hua, J. W.: Preliminary verification of  
838 instantaneous air temperature estimation for clear sky conditions based on SEBAL, *Meteorology and*  
839 *Atmospheric Physics*, 129, 71–81, <https://doi.org/10.1007/s00703-016-0451-3>, 2017.
- 840 Zhu, W. B., Lü, A. F., and Jia, S. F.: Estimation of daily maximum and minimum air temperature using  
841 MODIS land surface temperature products, *Remote Sensing of Environment*, 130, 62–73,  
842 <http://dx.doi.org/10.1016/j.rse.2012.10.034>, 2013.
- 843